AD741887

LIQUID INJECTION INTO A SUPERSONIC STREAM
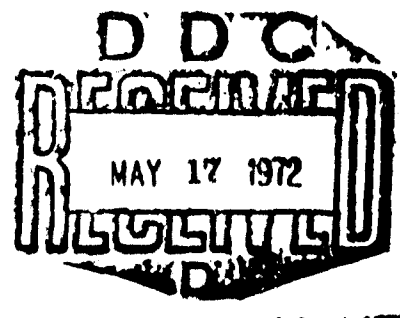
C. L. Yates

The Johns Hopkins University, Applied Physics Laboratory
Silver Spring, Md.

TECHNICAL REPORT AFAPL-TR-71-97 Vol. I
MARCH 1972

D D C
MAY 17 1972

AIR FORCE AERO PROPULSION LABORATORY
AIR FORCE SYSTEMS COMMAND
Wright-Patterson Air Force Base, Ohio

NOTICE

When Government drawings, specifications, or other data
are used for any purpose other than in connection with a
definitely related Government procurement operation, the
United States Government thereby incurs no responsibility
nor any obligation whatsoever; and the fact that the govern-
ment may have formulated, furnished, or in any way sup-
plied the said drawings, specifications, or other data, is
not to be regarded by implication or otherwise as in any
manner licensing the holder or any other person or cor-
poration, or conveying any rights or permission to manu-
facture, use, or sell any patented invention that may in any
way be related thereto.

Copies of this report should not be returned unless return
is required by security considerations, contractual obliga-
tions, or notice on a specific document.

LIQUID INJECTION INTO A SUPERSONIC STREAM

C. L. Yates

AIR FORCE AERO PROPULSION LABORATORY
AIR FORCE SYSTEMS COMMAND
Wright-Patterson Air Force Base, Ohio

DOCUMENT CONTROL DATA - R & D

Security classification of title, body of abstract and indexing annotation must be entered when the overall report is classified)

1. ORIGINATING ACTIVITY (Corporate author)	2a. REPORT SECURITY CLASSIFICATION
The Johns Hopkins University Applied Physics Lab. 8621 Georgia Ave. Silver Spring, Md. 20910	Unclassified
	2b. GROUP NA

3. REPORT TITLE

Liquid Injection Into A Supersonic Airstream

4. DESCRIPTIVE NOTES (Type of report and inclusive dates)

Final Report for Period January 1970 - September 1971

5. AUTHOR(S) (First name, middle initial, last name)

C. L. Yates

6. REPORT DATE	7a. TOTAL NO. OF PAGES	7b. NO. OF REFS
March 1972	98	21

8a. CONTRACT OR GRANT NO. N00017-72-C-4401	9a. ORIGINATOR'S REPORT NUMBER(S)
b. PROJECT NO. 3012	APL-TR-71-97 Vol. I
c. Task 30 1209	9b. OTHER REPORT NO(S) (Any other numbers that may be assigned this report)
d.	

10. DISTRIBUTION STATEMENT

Approved for public release; distribution unlimited.

11. SUPPLEMENTARY NOTES	12. SPONSORING MILITARY ACTIVITY
	Air Force Aero Propulsion Laboratory Wright-Patterson Air Force Base, Ohio 45433

13. ABSTRACT

Photographic data were obtained for the transverse injection of water and isopropyl alcohol from a flat-plate into airstreams having Mach numbers of 1.62 and 2.72. Jet/freestream dynamic pressure ratio, jet Reynolds and Weber numbers, and freestream Reynolds number were varied by factors of 8, 10, 11, and 3, respectively, in the jet penetration tests, and by factors of 23, 4, 9, and 5 in the jet spreading tests. Improved empirical equations for jet penetration and width were developed and were substantiated for two sets of test conditions by detailed flowfield mapping 50 jet diameters downstream using pitot-pressure, cone-static-pressure, and heated sampling probes. Since the injectant spatial distributions from the two tests were nearly similar on a nondimensionalized scale, it may be possible to use these data to predict distributions for other conditions. Finally, an improved theoretical analysis not only predicts jet penetration more accurately than previous ones, but also predicts the transverse distribution of injectant mass.

14.	KEY WORDS	UNCLASSIFIED

Scramjets
Jet Penetration
Liquid Injection

ABSTRACT

Photographic data were obtained for the transverse injection of water and isopropyl alcohol from a flat-plate into airstreams having Mach numbers of 1.62 and 2.72. Jet/freestream dynamic pressure ratio, jet Reynolds and Weber numbers, and freestream Reynolds number were varied by factors of 8, 10, 11, and 3, respectively, in the jet penetration tests, and by factors of 23, 4, 9, and 5 in the jet spreading tests. Improved empirical equations for jet penetration and width were developed and were substantiated for two sets of test conditions by detailed flow-field mapping 50 jet diameters downstream using pitot-pressure, cone-static-pressure, and heated sampling probes. Since the injectant spatial distributions from the two tests were nearly similar on a nondimensionalized scale, it may be possible to use these data to predict distributions for other conditions. Finally, an improved theoretical analysis not only predicts jet penetration more accurately than previous ones, but also predicts the transverse distribution of injectant mass.

THE JOHNS HOPKINS UNIVERSITY
APPLIED PHYSICS LABORATORY
SILVER SPRING, MARYLAND

FOREWORD

This unclassified report covers the results of the
work on liquid injection into a supersonic stream. This re-
port summarizes work conducted from January 1970 through
September 1971 with some reference to work conducted from
September 1968 through December 1969.

Technical management for the Air Force was under
Mr. John L. Leingang, Technical Manager, Advanced Com-
ponent Technology, Ramjet Technology Branch.

CONTENTS

CONTENTS (cont'd)

ILLUSTRATIONS

ILLUSTRATIONS (cont'd)

ILLUSTRATIONS (cont'd)

NOMENCLATURE

$\overline{A}$, A   local jet cross-sectional area; and dimensionless jet cross-sectional area, $A \equiv \overline{A}/\overline{A}_j$

C_d orifice discharge coefficient

C_D drag coefficient

C_p, C_{p_o} pressure coefficient, $C_p \equiv (p-p_\infty)/\overline{q}_\infty$; stagnation point pressure coefficient

d_e effective orifice diameter, $d_e \equiv C_d^{0.5} d_j$

d_j geometric orifice diameter

F_n normal force on jet element

$G(y)$, G_y percentage of injectant mass located at y; percentage of injectant mass located below y

m local mass of jet element

M Mach number

$\mathfrak{m}$ Molecular weight

$\vec{n}$ local coordinate normal to jet centerline

p static pressure

p_b pressure sensed by emerging jet

p_c cone-static pressure

p_t' pitot pressure

$\overline{q}$, q, q' dynamic pressure, $\overline{q} \equiv \rho V^2/2$; dynamic pressure ratio, $q \equiv \overline{q}_j/\overline{q}_\infty$; and ratio $q' \equiv \overline{q}_j/\overline{q}_s$

R jet centerline radius of curvature

$\mathfrak{R}$ gas constant

R_e Reynolds number, $R_e \equiv \rho V d_j/\mu$

$\vec{s},\ \bar{s},\ s$ local coordinate tangential to jet centerline; distance along $\vec{s}$; and dimensionless distance, $s \equiv \bar{s}/d_j$

T temperature

V velocity

$\bar{w},\ w$ local jet width; and dimensionless jet width, $w \equiv \bar{w}/d_j$

$\dot{w}$ mass flow rate

W_e Weber number $W_e \equiv \rho V^2 d_j/\sigma$

$\bar{x},\ x$ downstream distance from orifice center and dimensionless distance, $x \equiv \bar{x}/d_j$

X_i mole fraction of species i

$\bar{y},\ y$ vertical distance above flat-plate surface; and dimensionless distance, $y \equiv \bar{y}/d_j$

Y_i mass fraction of species i

$\bar{z},\ z$ lateral distance from orifice (flat-plate center-line); and dimensionless distance $z \equiv \bar{z}/d_j$

α local angle of jet centerline from horizontal

β jet breakup parameter

$\epsilon,\ \epsilon_0$ jet breakup variable; and jet breakup variable at initiation of disintegration

γ specific heat ratio

μ viscosity

φ angular displacement from jet stagnation point

$\bar{\rho},\ \rho$ density; and density ratio, $\rho \equiv \bar{\rho}_j/\bar{\rho}_\infty$

σ surface tension

Subscripts

A, R   species air and refrigerant-11 (injectant), respectively

B, C	jet boundary and centerline conditions, respectively
j	initial jet conditions
s	conditions after jet interaction shock
t	plenum conditions
∞	freestream conditions

SECTION I

INTRODUCTION

The fuel distribution achieved by transverse liquid injection into a supersonic airstream (Fig. 1) is of interest for the design of supersonic combustion ramjet engines. In prior experiments photographic techniques have generally been used to measure transverse penetration of the jet boundary for both subsonic (Refs. 1-3) and supersonic (Refs. 4-10)). gas streams, and/or jet boundary lateral spreading (Refs. 2, 5, 7, and 9-11). Ingebo's (Ref. 12) use of a mass-sampling probe is a singular case in which in-stream measurements have been previously applied to liquid injection. These past studies produced several empirical formulas for predicting jet penetration (Refs. 1, 2, 7, 9, and 12) and jet spreading (Refs. 2, 7, 9, and 11). Theoretical studies, however, have had the limited goal of predicting jet boundary penetration only. Theoretical models generally fall into two categories: those that assume the jet to be a solid body (Ref. 6) and those that include the effects of jet disintegration and distortion (Refs. 3, 8, and 13). The more successful models depend heavily upon empiricism.

The existing correlations and models often yield conflicting predictions of the absolute and relative importance of fluid properties such as injectant viscosity and surface tension. In fact, the ranges of conditions tested in many experiments are insufficient to allow the evaluation of property effects. The objectives of the present program were to advance the understanding of the problem of liquid injection by: (a) testing through wide ranges of system properties, (b) using more comprehensive experimental techniques to identify and evaluate the processes and properties that control the disintegration of a liquid jet column, and (c) relating these processes to the resultant spatial distribution of the injectant.

- 1 -
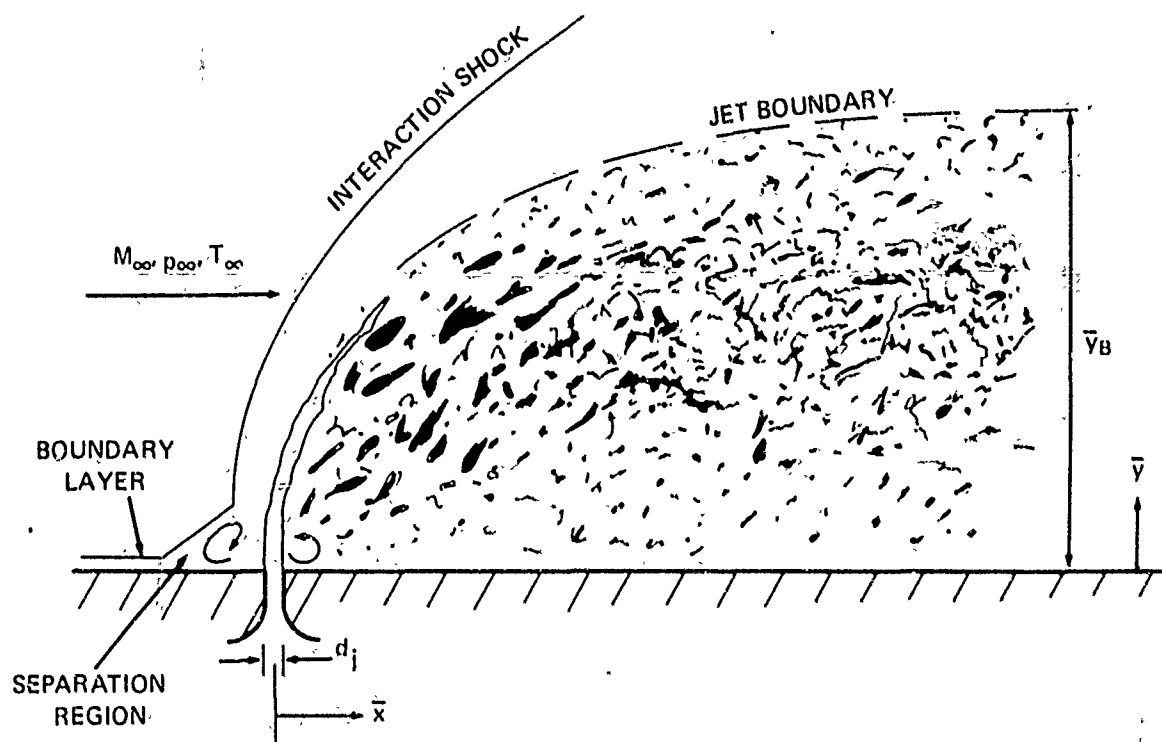
FIGURE 1   SCHEMATIC ILLUSTRATION OF LIQUID INJECTION INTO A SUPERSONIC STREAM

In the initial phase of this program, emphasis was put on the determination of jet boundary location by photographic techniques. Results obtained for jet penetration were previously reported in Ref. 14 and are only briefly summarized herein. The jet spreading results are presented herein, but they are also discussed in Ref. 14. Some photographic data for liquid injection obtained with a pulsed ruby laser are also discussed in this report.

The more recent effort in this program has been directed toward a determination of the detailed structure of a liquid jet flowfield using in-stream instrumentation. In particular, a mass-sampling probe was fabricated and evaluated, and together with pressure probes, applied to transverse liquid injection. The results of these tests have: (a) led to better understanding of liquid dispersion in a supersonic stream, (b) enabled a critical evaulation of existing empirical correlations and theoretical treatments, and (c) served as a basis for an improved theoretical analysis, as described herein.

SECTION II

EXPERIMENTAL SETUP AND MEASUREMENT
TECHNIQUES

A. TEST MODEL, INJECTANTS, AND TEST CONDITIONS

The stainless-steel, flat-plate model (Fig. 2) is
0.5-inch thick and 5 inches wide, with a 15° leading-edge
angle and a 10.5-inch working length. A removable injec-
tor insert is located 3.06 inches from the leading edge in
a plenum that is fed by two holes drilled 180° apart, from
opposite sides of the plate. The geometrically similar in-
ternal flow passage of each of the injector inserts consists
of a cylindrical exit section (diameter = length = d_j) that
is connected by a transition section (blending radius =
$2 d_j$) to a cylindrical inlet section (diameter = $5 d_j$). Injec-
tant pressure and temperature are measured in the plenum.

The liquid supply system provides for remote,
nitrogen-pressurization up to 1500 psi, and flow rate mea-
surement via a turbine flow meter. Some pertinent prop-
erties of the liquids are listed in Table 1.

Table 1

Liquid Properties (at 20°C unless stated otherwise)

Liquid	Density (gm/cm³)	Viscosity (cp)	Surface Tension (dynes/cm)	Vapor Pressure (mm Hg)	Boiling Tempera- ture (°C)	Heat of Vaporiza- tion (cal/gm *)
Water	0.998	1.005	72.8	17.54	100.0	539.6
Isopropanol	0.785	2.370	21.7	22.07	82.4	159.4
Refrigerant-11	1.464*	0.405**	19.0†	672.0	23.8	43.5

* at boiling temperature

** at 30°C

† at 25°C

Preceding page blank

INJECTOR ORIFICE

FLAT PLATE

M 2.72 NOZZLE

LIQUID SUPPLY LINE

SUPPORT STRUT
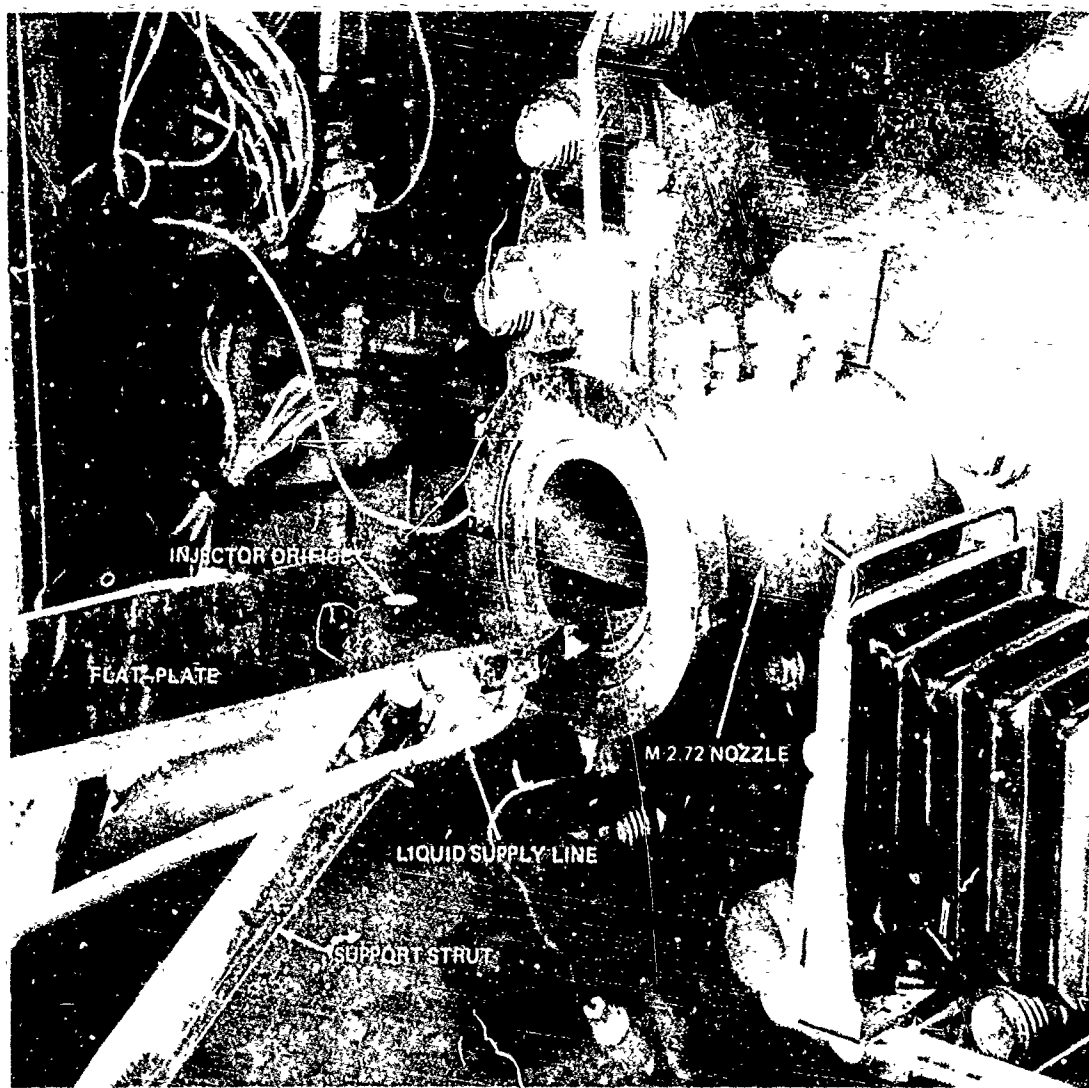
FIGURE 2   JET PENETRATION TEST APPARATUS

For water and isopropanol, temperature-dependent properties were used in reported calculations. A bothersome feature with refrigerant-11 is that the injector will become partially plugged with ice if either the liquid supply system or the air supply contains water. Extreme care had to be exercised to avoid ice formation, which could be sensed by a variation in the injectant flow rate for a given injectant plenum pressure.

Table 2 lists the test conditions for the tests discussed herein. The tests are conducted in a 2.74-inch-diameter, free-air jet from a contoured-supersonic (Mach 1.62 or 2.72) nozzle. The values listed for the effective injectant orifice diameter d_e are based on calibration tests, in which the orifice discharge coefficient C_d was measured for Re_j between 4.5×10^3 and 1×10^5. In those tests, liquids were injected into a quiescent medium, and the metered flow rate was compared with the ideal value computed by the Bernoulli equation.

B. PHOTOGRAPHIC TECHNIQUES

The photographic data for jet penetration were obtained by direct-luminosity, 16-mm cine-photographs (31-ms exposure). Comparisons with data from 70-mm schlieren photographs using both 20-ms and 0.25-μs (spark) exposures showed that variances in measured penetration height of as much as 40% could result from different photographic techniques. These results pointed up the difficulty of using photographic data to establish any weak dependency of penetration on injectant or freestream properties and indicated that care must be exercised in comparing results from different experiments. The jet spreading data were obtained by direct-luminosity, 4- by 5-inch still photographs (2.5 ms exposure).

The 70-mm, direct-luminosity laser photographs were obtained using a Q-switched ruby laser having a nominal rating of ~ 150 MW, with a pulse width of ~ 20 ns.

Table 2
Experimental Conditions

Test	Injectant	d_j (in)	d_e (in)	M_∞	P_{t_∞} (psia)	T_{t_∞} (°R)	P_{t_j} (psia)	T_{t_j} (°R)	V_∞ (ft/s)	V_j (ft/s)	q	$Re_\infty \times 10^{-4}$	$Re_j \times 10^{-4}$	$We_j \times 10^{-4}$
a) Jet penetration tests														
1 (a)(b)	Water	0.0262	0.0253 / 0.0255	2.72	358 / 359	952 / 957	270 / 838	560 / 574	2611 / 2618	200 / 347	3.48 / 10.30	6.36 / 6.31	5.50 / 11.10	3.53 / 10.70
2	Water	0.0262	0.0256	2.72	359	959	857	619	2621	348	10.30	6.29	16.50	11.40
3	Water	0.0262	0.0257	2.72	352	1362	976	628	3123	270	11.80	3.92	19.60	13.00
4 (a)(b)(c)	Isopropyl alcohol	0.0262	0.0247 / 0.0249 / 0.0251	2.72	355 / 353 / 354	951 / 959 / 966	334 / 612 / 925	553 / 553 / 557	2610 / 2621 / 2631	234 / 319 / 390	3.75 / 6.97 / 10.40	6.50 / 6.19 / 6.15	1.99 / 2.76 / 3.63	12.70 / 23.70 / 35.50
5 (a)(b)(c)	Water	0.052	0.0507 / 0.0509 / 0.0510	2.72	354 / 352 / 352	983 / 962 / 967	294 / 654 / 928	566 / 566 / 566	2654 / 2625 / 2362	206 / 310 / 367	3.70 / 8.46 / 11.90	11.90 / 12.60 / 12.10	12.10 / 18.40 / 21.90	7.42 / 16.90 / 23.70
6 (a)(b)(c)	Water	0.0262	0.0252 / 0.0254 / 0.0255	1.62	65 / 64 / 65	950 / 939 / 931	317 / 599 / 917	566 / 572 / 564	1981 / 1970 / 1961	205 / 278 / 342	10.30 / 19.20 / 28.80	2.01 / 2.01 / 2.05	5.95 / 8.70 / 9.93	3.70 / 6.88 / 10.30
b) Jet spreading tests														
7 (a)(b)(c)(d)	Isopropyl alcohol	0.027	0.0233 / 0.0249 / 0.0255 / 0.0257	2.72	344 / 345 / 344 / 345	468 / 467 / 468 / 468	118 / 318 / 619 / 925	494 / 501 / 504 / 504	1831 / 1829 / 1831 / 1831	133 / 228 / 320 / 395	1.3 / 3.8 / 7.4 / 11.2	17.50 / 17.64 / 17.50 / 17.55	0.38 / 0.83 / 1.30 / 1.62	3.98 / 11.76 / 23.32 / 35.46
8 (a)(b)(c)	Isopropyl alcohol	0.027	0.0236 / 0.0247 / 0.0256	1.62	65 / 66 / 67	452 / 449 / 451	134 / 325 / 926	492 / 492 / 497	1367 / 1362 / 1365	148 / 235 / 396	4.5 / 10.8 / 30.1	5.60 / 5.77 / 5.79	0.41 / 0.71 / 1.42	4.90 / 12.32 / 35.30
9 (a)(b)	Isopropyl alcohol	0.017	0.0142 / 0.0150	1.62	67 / 66	450 / 449	317 / 913	492 / 490	1364 / 1362	229 / 390	10.0 / 29.7	3.55 / 3.52	0.38 / 0.69	7.10 / 20.61
c) Laser-photography tests														
10 (a)(b)(c)	Refrigerant-11	0.027	0.0262 / 0.0263 / 0.0264	1.62	66	514	107 / 232 / 703	532	1459	92 / 138 / 234	3.2 / 7.1 / 20.6	4.70	6.73 / 10.16 / 17.41	4.33 / 9.76 / 28.30
d) In-stream probe tests														
11	Refrigerant-11	0.027	0.0263	2.72	354	525	211	540	1940	134	2.3	14.98	9.71	8.89
12	Refrigerant-11	0.027	0.0265	2.72	354	525	905	540	1940	282	10.3	14.59	20.59	39.11
13	Refrigerant-11	0.052	0.0508	2.72	351	525	302	535	1939	153	3.1	28.62	21.54	22.42

The 9/16-inch-diameter beam was expanded sufficiently
to give complete coverage of the subject and the correct
exposure for the Linagraph Shellburst (red sensitive) film;
the beam was not recollimated. To decrease the effect of
ambient light without the use of extensive shielding pro-
cedures, the laser was triggered by a motorized camera
that had a 20-ms shutter window.

C. MASS-SAMPLING SYSTEM AND PRESSURE PROBES

The main requirements for a sampling system for
use in a heterogeneous stream are that it extract a repre-
sentative sample from the stream and prevent condensa-
tion and entrapment of liquid on components of the system
during the collection and analysis stages. For this pur-
pose, the heated probe shown in Fig. 3 was fabricated
and evaluated. Its tip consists of concentric stainless
steel tubes separated by an aluminum oxide insulator. The
steel tubing serves as the conductor in an electric circuit
powered by a 12-volt battery, and the entire length of the
probe and tubing to the sample container is heated. The
probes are mounted in a three-point rake with a 0.281-
inch center-to-center spacing (Fig. 4). The sample con-
tainers are wrapped with heating tape, so that subsequent
analysis can be made by gas chromatography. The gas
chromatograph was extensively modified to assure that all
internal passages are kept warm enough to avoid condensa-
tion within the unit.

The remaining in-stream instrumentation consisted
of pitot-pressure and cone-static-pressure rakes, the
most recent versions of which are shown in Fig. 5. The
five-point pitot rake used 0.065-inch OD by 0.047-inch-
ID steel tubing spaced at 0.281 inch center-to-center. The
three 0.125-inch OD, cone-static-pressure probes are
spaced at 0.562-inch center-to-center. Each has a 15°
half-angle cone, with four 0.015-inch-diameter, equally-
spaced pressure ports located 0.170-inch from the tip
and connected to individual strain-gauge pressure trans-
ducers.

DIMENSIONS ARE IN INCHES

SILVER
SOLDER

304 STAINLESS STEEL TUBE
0.109 OD BY 0.012 WALL

ELECTRICAL
CONNECTIONS

15°

0.010
DIAMETER

ALUMINUM OXIDE TUBE
0.078 OD BY 0.008 WALL

304 STAINLESS STEEL TUBE
0.058 OD BY 0.008 WALL

PROBE RAKE BODY
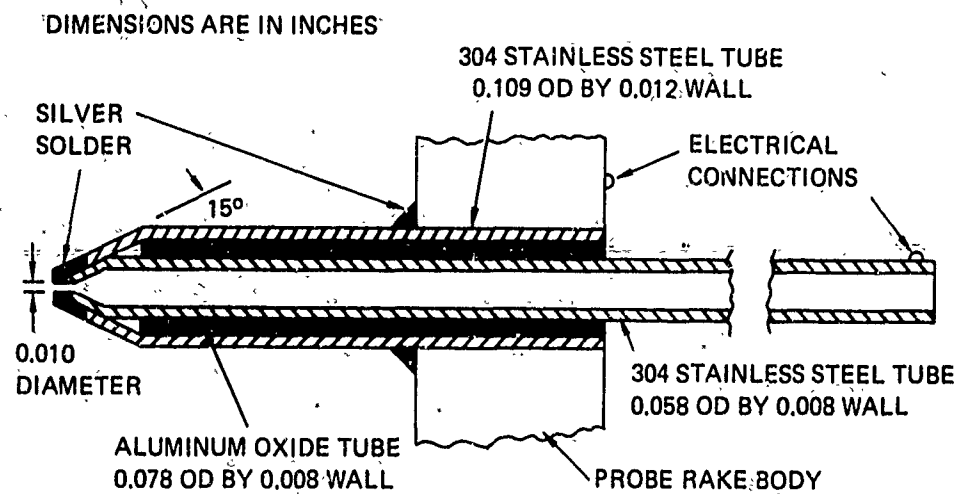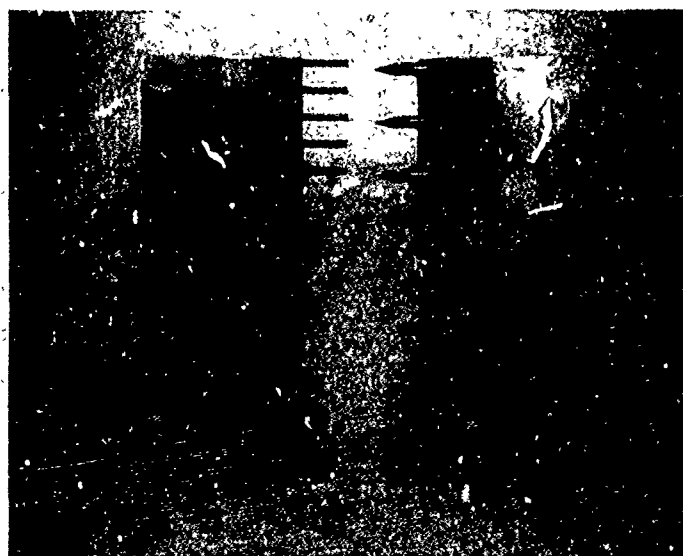
FIGURE 3   HEATED MASS-SAMPLING PROBE SCHEMATIC

FIGURE 4   TWO-PHASE MASS-SAMPLING PROBE

PITOT PROBE   CONE-STATIC PROBE

FIGURE 5   PHOTOGRAPH OF PRESSURE PROBES

- 11 -

SECTION III

EXPERIMENTAL RESULTS FROM PHOTOGRAPHY

A. SUMMARY OF PHOTOGRAPHIC JET PENETRATION RESULTS

In the jet penetration studies (Ref. 14), tests were made for a set of reference conditions that were arbitrarily chosen as follows:

Water injection: $d_j = 0.0262$ inch; $T_{t_j} \approx 570°R$

Airstream: $M_\infty = 2.72$; $T_{t_\infty} \approx 960°R$;

$p_\infty = 14.9$ psia.

A series of tests was then made in which injectant type, T_{t_j}, T_{t_∞}, d_j, and M_∞ were successively varied; in most tests, some variation of p_{t_j} between ≈ 300 and ≈ 900 psia was obtained. Our results (Fig. 6, column A) showed that the parameter $\bar{y}_B/d_e q^{0.5}$ almost collapses the data for various q's in a given test to a single curve, and the deviations from a single curve have a random nature. Moreover, data for about the same q (Fig. 6, column B) showed no consistently clear effect on $\bar{y}_B/d_e$ of any other system parameter in the form of either Reynolds or Weber numbers or physical properties of the fluids. When our data are put on a single graph as in Fig. 7, the data spread is nearly constant for all values of $\bar{x}/d_e$, and the following equation fits the data to within ± 10% in the region $\bar{x}/d_e \geqslant 20$:

$$\bar{y}_B/d_e = 1.1\ q^{0.5}\ \ell n\ (1 + 10\ \bar{x}/d_e) . \tag{1}$$

The logarithmic form of Eq. (1) was suggested by two circumstances: (a) log-log plots of $\bar{y}_B/d_e$ versus $\bar{x}/d_e$ showed
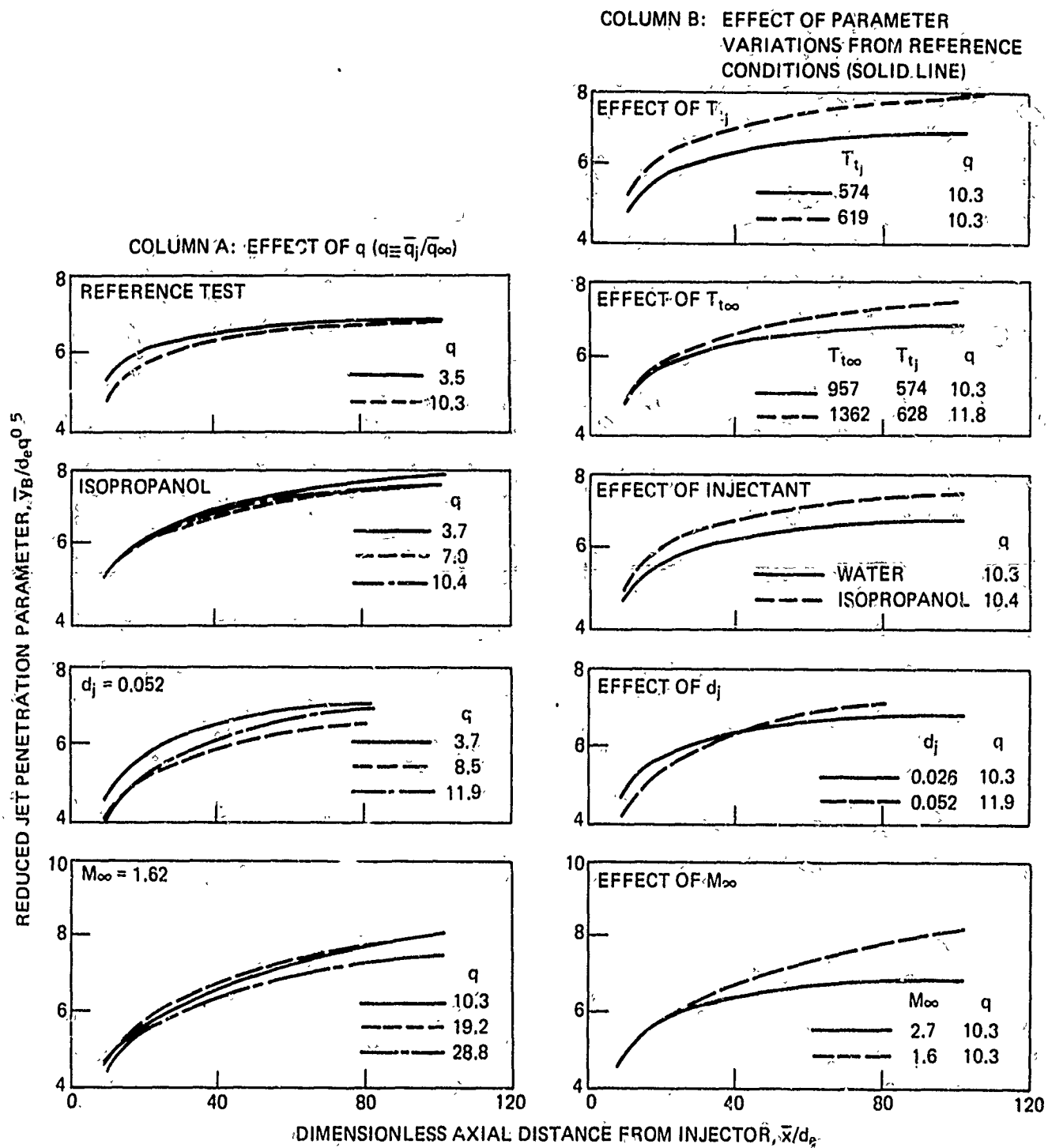
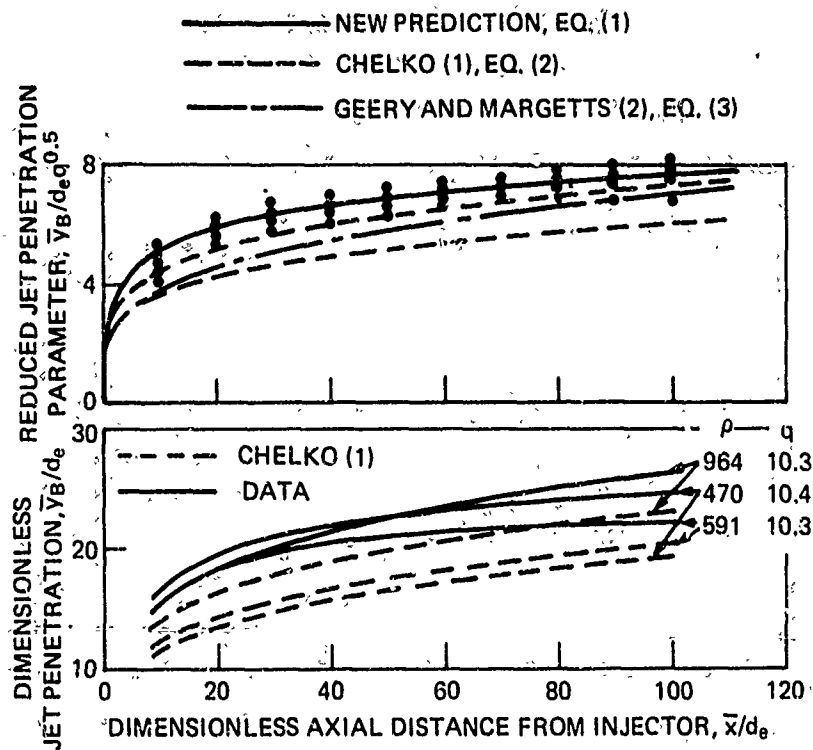FIGURE 6 EFFECT OF VARIATION OF PARAMETERS ON JET PENETRATION

- 14 -

FIGURE 7   COMPARISONS OF EMPIRICAL PREDICTIONS TO PRESENT DATA
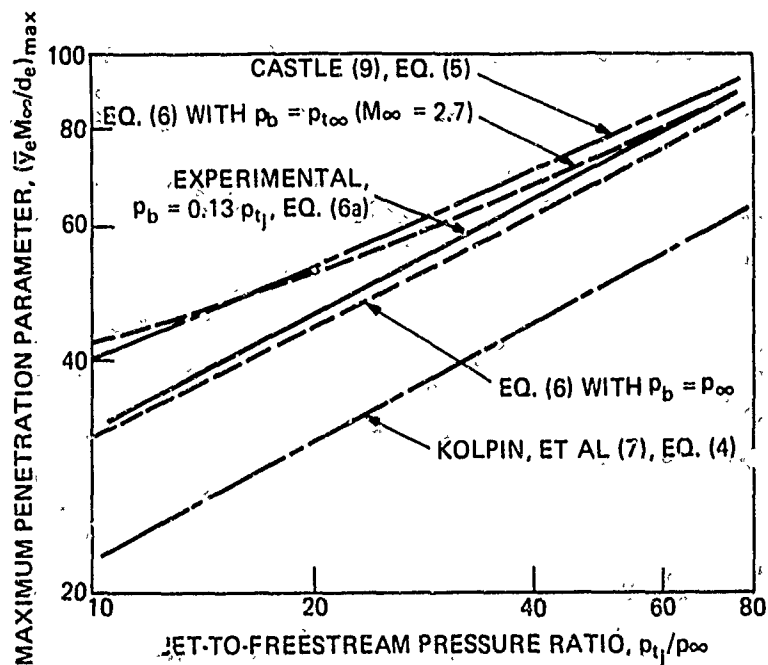

FIGURE 8   COMPARISONS OF EMPIRICAL PREDICTIONS FOR
PENETRATION AT x = 150 TO PRESENT DATA

- 15 -

that significant curvature remained in the trajectory curves, and (b) the logarithmic form often results in theoretical studies of liquid injection (see Section V). The equation is compared to the jet penetration results obtained by instream mass-sampling in Section IV.

Our jet penetration data are in fair agreement with some previously derived empirical correlations. The following two from Refs. 1 and 2, respectively, predict that $\bar{y}_B$ varies with $\bar{x}$ and q according to simple power laws:

$$\bar{y}_B = 0.45 \, \rho^{0.265} \, q^{0.475} \, x^{0.22} \, , \tag{2}$$

$$\bar{y}_B = 2.0 \, q^{0.5} \, x^{0.27} \, . \tag{3}$$

[Note that Eqs. (2) and (3) are scaled in terms of d_j, rather than d_e; hence, $C_d = 1$ is assumed in the comparisons.] Equations (2) and (3) are compared with the data in Fig. 7, where the two curves shown for Eq. (2) are based on the extreme values of ρ and q that existed in our tests. In view of typical photographic data bias, the quantitative predictions of Eqs. (2) and (3) compare favorably to the data. However, the power-law dependency of $\bar{y}_B$ on $\bar{x}$ gives poorer overall qualitative agreement. In addition, the ρ dependency predicted in Eq. (2) is not supported by the present data, as seen in the lower part of Fig. 7, which compares trajectories for which ρ was varied but the q's were nearly equal.

The following correlations from Refs. 7 and 9, respectively, predict that maximum $\bar{y}_B/d_e$ always occurs by $\bar{x}/d_e = 150$ and is given by:

$$(\bar{y}_B/d_e)_{max} = (6.77/M_\infty)(p_{t_j}/p_\infty)^{0.51} \, , \tag{4}$$

$$(\bar{y}_B/d_e)_{max} = (15.7/M_\infty)(p_{t_j}/p_\infty)^{0.407} \, . \tag{5}$$

In order to compare Eqs. (4) and (5) to our data, which were limited to $\bar{x}/d_e < 100$, Eq. (1) was evaluated for $\bar{x}/d_e = 150$, and, using the Bernoulli equation and the definition of q, rewritten as follows:

$$(\bar{y}_B/d_e)_{max} = (9.62/M_\infty)\,[(p_{t_j} + p_b)/p_\infty]^{0.5}, \qquad (6)$$

Equation (6) is compared with Eqs. (4) and (5) in Fig. 8, where two cases of the back pressure sensed by the jet are considered: $p_b = p_\infty$, and $p_b = p_{t_\infty}'$, where p_{t_∞}' is the freestream pitot pressure. These two cases bracket the experimental p_b's, which roughly agreed with the expression:

$$\bar{p}_b \approx 0.13\,p_{t_j}. \qquad (7)$$

This latter expression allows Eq. (6) to be written as:

$$(\bar{y}_B/d_e)_{max} \approx (10.2/M_\infty)\,(p_{t_j}/p_\infty)^{0.5}. \qquad (6a)$$

Equation (6a), which approximately represents the data, also is shown in Fig. 8 to fall between Eqs. (4) and (5). It is in closer qualitative agreement (slopes) with the former, but is in closer quantitative agreement with the latter. In fact, the predictions of Eq. (5) are 50 to 70% higher than those of Eq. (4) for the range of conditions covered in our tests. It is apparent from the comparisons of Eq. (1) [which lead to the approximation (6a)] with Eqs. (4) and (5) that the use of p_{t_j}/p_∞ as an independent variable is essentially equivalent to the use of q for the ranges of conditions normally encountered in liquid injection. However, the frequent and natural appearance of q in analytical studies suggests that the use of q in empirical correlations is more justifiable.

From our data, it was established that a superior correlation was obtained with d_e, as opposed to d_j, as the

- 17 -

length scale. This is apparently due to the fact that the use of d_e partially accounts for the boundary layer of the emerging jet, which depends upon the internal geometry of the injector. In fact, an effective diameter based on momentum flow considerations would be even more appropriate than the present d_e, which is based on mass flow considerations.

B. PHOTOGRAPHIC STUDIES OF JET BOUNDARY SPREADING

Effects of d_j (0.017 and 0.027 inch), p_{t_j} (118 to 926 psia), and M_∞ (1.62 and 2.72) on the spreading of isopropanol jets were determined. Still photographs of 2.5-ms exposure (Fig. 9) were obtained by recording the back-scattered light from flood lamps located above the flat-plate surface. The data were subject to variations up to 25% as a result of individual interpretation of the jet boundary location. It was possible to make measurements at $(\overline{z}_B/d_e)$'s up to $\approx$ 70 for d_j = 0.027 inch and up to $\approx$ 125 for d_j = 0.017 inch.

The typical results in Fig. 10 show that, for given d_j and M_∞, $\overline{z}_B/d_e$ increases with p_{t_j} for $\overline{x}/d_e \geqslant$ 10; however, in some cases, the opposite trend is observed for small $(\overline{x}/d_e)$'s (this behavior at M_∞ = 2.72 can be seen in Fig. 10, where the leading edge of the jet at p_{t_j} = 118 psia is notice-ably blunter for $\overline{x}/d_e \leq$ 5). For given d_j and p_{t_j}, $\overline{z}_B/d_e$ decreases with M_∞ for $\overline{x}/d_e \geqslant$ 3 but increases with M_∞ for smaller $\overline{x}/d_e$'s. This behavior suggests that initial jet spreading is controlled by dynamic and/or viscous forces that the airstream imposes within the stagnation region of the jet column, tearing ligaments or drops from the jet and imparting lateral momentum to them. These initial spreading effects are greater when M_∞ increases and when the mean vertical momentum of the jet is smaller (lower p_{t_j} for given d_j) or when the jet has a lower Re_j and, hence a relatively larger boundary layer (smaller d_e for given p_{t_j}). Having been torn away, the drops are subjected to

- 18 -

AIRFLOW⟶

(a) $P_{t_j} = 118$ PSIA, $M_\infty = 2.72$

(b) $P_{t_j} = 925$ PSIA, $M_\infty = 2.72$

(c) $P_{t_j} = 926$ PSIA, $M_\infty = 1.62$

| 0 | 20 | 40 | 60 |

$\bar{x}/d_j$

FIGURE 9   PHOTOGRAPHS OF JET SPREADING FROM 0.027-INCH ORIFICE

- 19 -

(a) EFFECTS OF INJECTION PRESSURE AND FREESTREAM MACH NUMBER

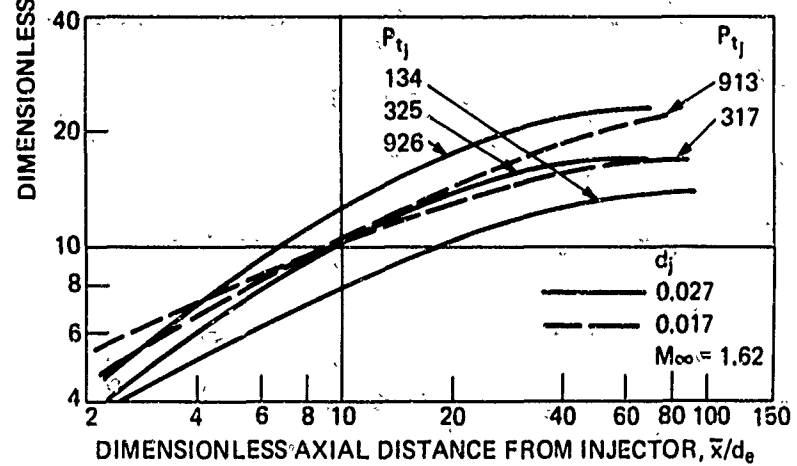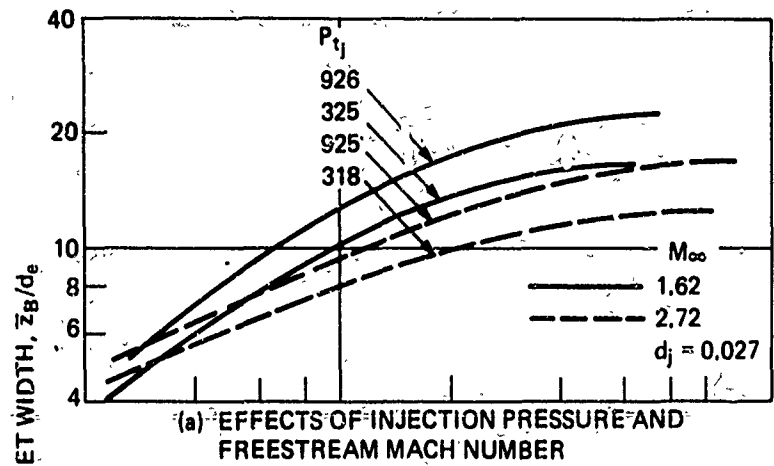(b) EFFECTS OF INJECTION PRESSURE AND ORIFICE DIAMETER

FIGURE 10   TYPICAL JET SPREADING RESULTS

- 20 -

dynamic forces imposed by the freestream. Since the resulting axial momentum interchange also increases with M_∞, the ultimate spreading decreases for an increase in M_∞.

The only substantial efforts to correlate jet spreading data have been directed toward predicting the maximum jet width $\bar{z}_{B_{max}}/d_e$, which is assumed to occur by $\bar{x}/d_e = 150$. (Note that the change in character of jet width versus system parameters with increasing $\bar{x}$ requires a rather complicated expression to predict the entire boundary trajectory.) Initially, the correlations were in the form $\bar{z}_{B_{max}}/d_e \propto (p_{t_j}/p_\infty)^c$, where c was determined as 0.133 and 0.197 in Refs. 7 and 9, respectively. Photographic data were obtained in Ref. 7 for water injection into a Mach 2.8 airstream with d_e's of 0.0117 to 0.0211 inch. The correlation from Ref. 9 was based on photographic data for the injection of water, heptane, and a 58% glycerin-42% water solution into Mach 2.8 and Mach 4.0 air streams from orifices with d_e's of 0.0117 to 0.0624 inch. In Ref. 11, the correlation was modified to include a Mach number dependency:

$$\bar{z}_{B_{max}} M_\infty^{0.5}/d_e = 45 (p_{t_j}/p_\infty)^{0.133} . \qquad (8)$$

The present data are compared to Eq. (8) in Fig. 11, which includes some typical data points from Ref. 9 for injection of water, heptane, and a water-glycerin solution. To make the comparison, it was necessary to extrapolate some of the spreading data curves to determine $\bar{z}_{B_{max}}/d_e$. However, such extrapolation was reasonably safe, since the slopes of the curves in Fig. 10 had become very small at $\bar{x}/d_e > 60$. The present data (open symbols in Fig. 11) are represented well ($\pm 7.5\%$) by a single straight line, but the equation for this line is:

$$\bar{z}_{B_{max}} M_\infty^{0.5}/d_e = 10.4 (p_{t_j}/p_\infty)^{0.25} . \qquad (9)$$
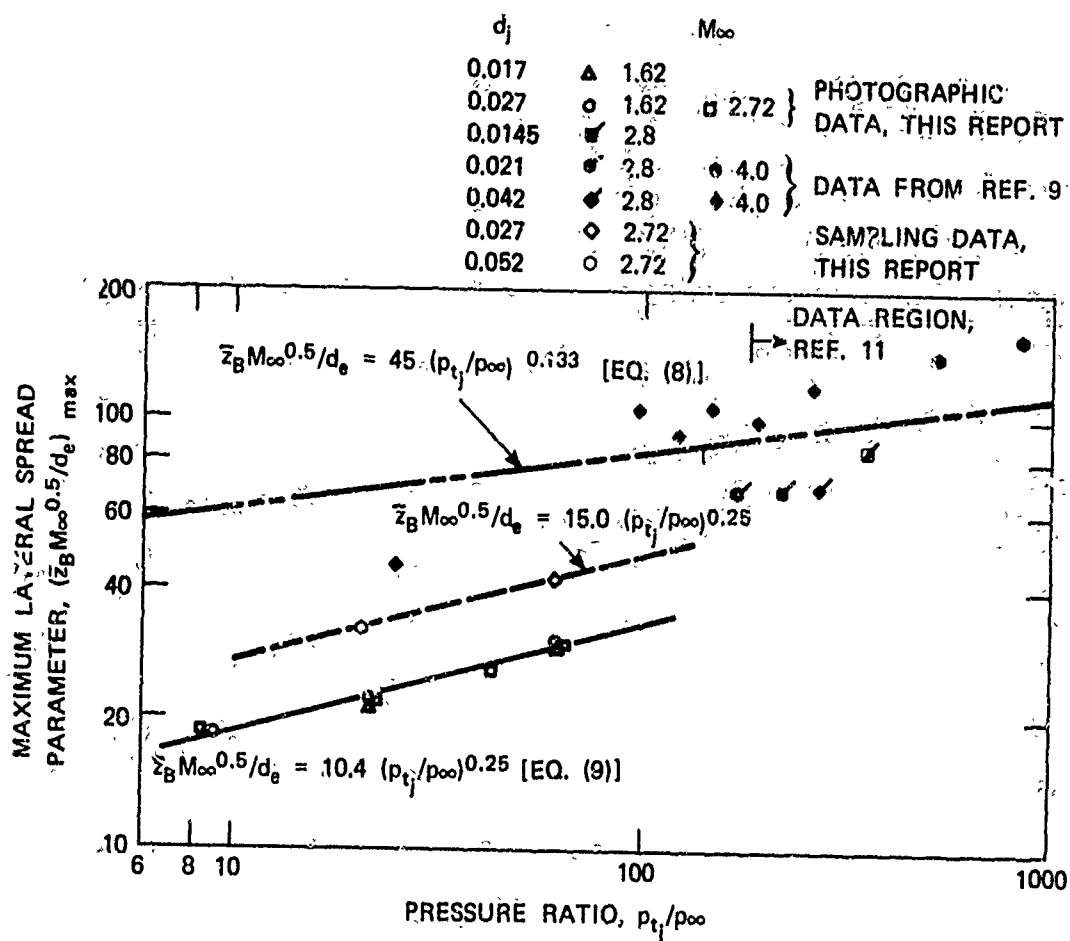
- 21 -

FIGURE 11   COMPARISON OF JET SPREADING DATA TO EXISTING DATA AND
CORRELATION

Equation (8) predicts jet widths that are higher than the present data by factors of ≈ 2 (at $p_{t_j}/p_\infty = 1000$) to ≈ 3.3 ($p_{t_j}/p_\infty = 10$). However, owing to the considerable data scatter, a line having a 0.25 slope does not violate the Ref. 9 data.

Mass-sampling data at $\bar{x}/d_e = 51$ for refrigerant-11 with $M_\infty = 2.72$ that are discussed later yield $\bar{z}_B M_\infty^{0.5}/d_e = 36.3$ for $p_{t_j}/p_\infty = 61.4$, and $\bar{z}_B M_\infty^{0.5}/d_e = 27.9$ for $p_{t_j}/p_\infty = 20.7$. From the $M_\infty = 2.72$ results shown in Fig. 10, it is judged that $\bar{z}_B$ would increase by no more than 10% in going from $\bar{x}/d_e = 51$ to the point where $\bar{z}_{B_{max}}/d_e$ occurs. Even if a 15% increase were accepted, upper limits for these two data points, which are plotted in Fig. 11, would be 41.7 and 32.1 at $p_{t_j}/p_\infty = 61.4$ and 20.7, respectively.

A line through these points still has a slope of 0.25, but a constant of 15.0, compared to the 10.4 in Eq. (9). Relative to this dashed line, predictions from Eq. (8) would still be > 84% high for the range of the present data, and as much as 67% high for the data region ($p_{t_j}/p_\infty > 150$) on which Eq. (8) is based.

If the procedure used to derive Eq. (6a) from Eq. (1) were applied inversely to Eq. (9), there would result: $\bar{z}_B/d_e \propto q^{0.25}$. In fact, the present photographic data are equally well correlated ($\pm 7.5\%$) by

$$\bar{z}_B/d_e = 10 \, q^{0.25} \, . \tag{10}$$

In any event, the correlations found for $\bar{y}_{B_{max}}/d_e$ and $\bar{z}_{B_{max}}/d_e$ combine to give $\bar{y}_{B_{max}}/d_e \approx 0.08 \, (\bar{z}_{B_{max}}/d_e)^2$.

C. LASER PHOTOGRAPHS OF LIQUID INJECTION

The object of the laser-photography studies was to determine whether the flowfield could be sufficiently

- 23 -

stopped to allow identification of individual fluid particles. Figure 12 shows direct-luminosity photographs obtained with the camera set at f/4.5, with a 1.06:1 magnification. Parts a and b show results for identical test conditions at different times, and parts c and d show results for a lower and a higher injection pressure, respectively. (The probes seen in the photographs are not in the jet flowfield. The reflection of the jet flow is also seen in the flat-plate surface.) These pictures show the unsteadiness of the flow and the irregular shape of the outer jet boundary. These features had been noted previously using a 250-ns spark source, as compared to ~ 20 ns for the laser; however, the laser photographs show considerable more detail within the jet core, and one can clearly see variations of the injectant density over the flowfield. The jet remains essentially intact for some distance before its breakup begins, which results in a region behind the jet and near the plate surface that is nearly devoid of injectant (farther downstream, fluid mixing eventually eliminates this region). Unfortunately, the number of fluid particles is too large to permit them to be identified individually. It seems doubtful that the more sophisticated holographic techniques would solve this problem either.
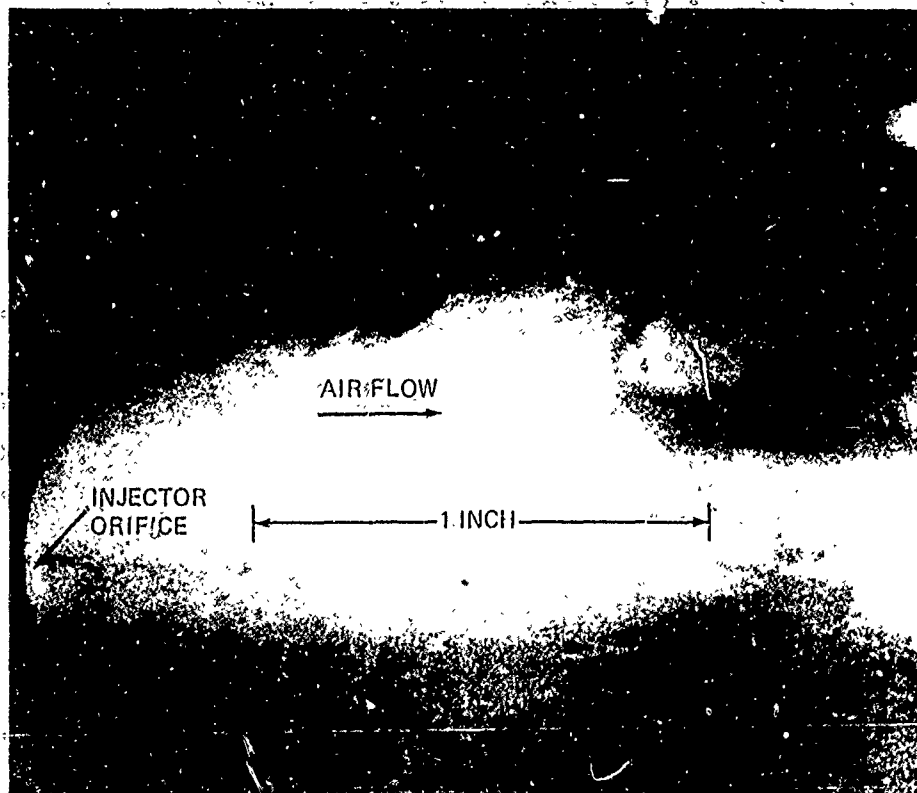
(a) TEST 10 (b): d_j = 0.027 INCH M_∞ = 1.62 p_{tj} = 232 PSIA   TIME: t

(b) TEST 10 (b)   TIME : t + Δt

FIGURE 12   PHOTOGRAPHS OF LIQUID INJECTION FLOWFIELD USING PULSED RUBY LASER

(c) TEST 10 (a): d_j = 0.027 INCH M_∞ = 1.62 p_{t_j} = 107 PSIA

(d) TEST 10 (c): d_j = 0.027 INCH M_∞ = 1.62 p_{t_j} = 703 PSIA

FIGURE 12 (CONCLUDED)

SECTION IV

IN-STREAM FLOWFIELD MEASUREMENTS

A. EVALUATION OF MASS-SAMPLING SYSTEM

It was recognized early in this program that:

    1. The spatial distribution of the injected mass must be known if one is to characterize completely the injection process;

    2. Standard photographic techniques are not sensitive enough to permit an evaluation of the effects of injectant properties such as viscosity and surface tension on this spatial distribution; and

    3. Measurements of this spatial distribution would improve the understanding of the controlling mechanisms and form the basis for realistic theoretical models of liquid injection.

    In some early tests a refrigerant-22 (chlorodifluoromethane) jet was sampled with an unheated probe, and it was found that, on the jet centerline, the maximum injectant composition occurred at a height that was only 40% of the maximum penetration. The use of an unheated probe was permissible in those tests because the high vapor pressure of refrigerant-22 assured that it would rapidly vaporize in the airstream and not condense in the sampling system. To test less volatile liquids, it was necessary to develop the heated sampling system. The probe design and use of an insulated and warmed gas chromatograph were described in Section IIC.

    To evaluate the sampling system, premixed samples of known composition were collected and analyzed. The test apparatus (Fig. 13) for preparing the sample

AIR SUPPLY   AIR METERING VENTURI

AIR HEATER (ELECTRICALLY HEATED NICKEL TUBE)

PRESSURE REGULATOR

81 INCHES

SAMPLING RAKE

1 INCH PIPE (1.06-INCH ID)

SPRAY NOZZLE (CONTRA STREAM INJECTION)

N₂ SUPPLY

PRESSURE REGULATOR

TO SAMPLE BOTTLES

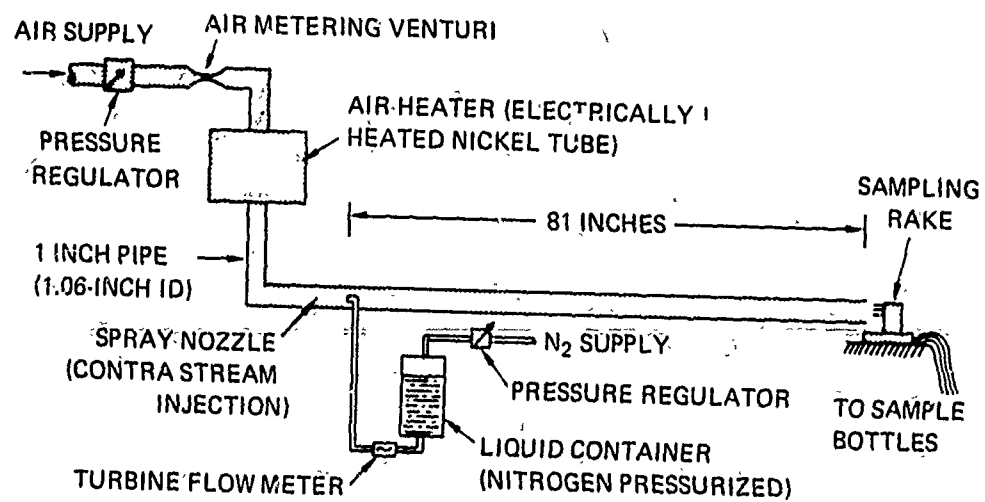LIQUID CONTAINER (NITROGEN PRESSURIZED)

TURBINE FLOW METER

FIGURE 13   SCHEMATIC OF TEST APPARATUS FOR MASS-SAMPLING PROBE EVALUATION

employed contra-stream injection of a metered liquid flow
via a spray nozzle into a metered airstream that could be
heated to 500°F. Vaporization and mixing occurred in a
1.06-inch-diameter, 81-inch-long pipe. The mixture is
discharged either directly from the pipe as a subsonic
stream, or from a 1.3-inch-exit-diameter, Mach 2 noz-
zle. In the initial tests, subsonic, isopropanol-air mix-
tures were sampled and analyzed as being more than 30%
lower than the input values. These results led to a deci-
sion to use the more volatile refrigerant-11 (trichloro-
fluoromethane), which boils at 75°F and reduces heating
requirements on the sampling equipment.

The results with refrigerant-11 are summarized in
Table 3. Tests A-I were conducted with heated air to avoid
condensation of the mixture on pipe wall surfaces. Except
for the supersonic Test E, the sampled mass percent was
lower than the input value. The errors for the subsonic
tests varied from -8 to -17% for the supersonic tests,
from 6 to 7%. However, samples taken from different
points of the stream usually were in close agreement,
suggesting thorough mixing of the stream. No consistent
dependence of sampling error on the input mass percent
level was observed.

Table 3

Summary of Mass-Sampling Probe Evaluation
Tests with Refrigerant-11

Test	Mach No.	Mixture Total Temperature (°R)	Liquid Input Mass Percent	Probe Location*	Sampled Mass Percen	Error (%)
A	< 1	750	29.6	0.33 R	24.8	-16
B	(pipe)		29.2	0.67 R	24.2	-17
C			62.4	0.33 R	57.1	- 9
D			62.1	0.67 R	57.4	- 8
E	2.0	600	39.8	0	42.5	+ 7
F	(nozzle)			0.58 R	38.6	- 3
G		660	47.2	0	44.8	- 5
H				0.58 R	45.2	- 4
I			53.9	0.33 R	50.7	- 6
J	2.0	490	57.4	0	75.0	+31
K	(no heat)			0.58 R	65.6	+14
L			67.1	0	88.9	+33
M				0.58 R	78.5	+17

*Radius fraction from centerline in pipe or nozzle exit plane.

When the mass-sampling system was used in jet penetration tests in which unheated air was used (these results are described later), the results suggested that the sampled mass fraction was incorrectly high. To assess these findings, evaluation tests J-M in Table 3 were conducted with unheated air. Indeed, the sampling errors (+14 to +33%) were greater and in the opposite direction from those determined with heated air. In addition, the compositions measured at 0.58 R were 10 mass percent lower than those measured at the centerline, which suggested that the test stream was nonuniform, due to either insufficient mixing or condensation on the pipe wall surfaces. If, in these evaluation tests (and the jet penetration tests described later), a significant portion of the injectant remained in the liquid phase, either or both of two effects might cause the erroneously high results: (a) liquid drops could intermittently plug the probe, blocking the air flow into it; and (b) if the shock wave on the sampling probe were detached, the centrifugal forces created by the shock could cause the lighter air component of the flow to be deflected by a larger amount, resulting in disproportionately large amount of the injectant (both liquid and gaseous) entering the probe.

While the performance of this probe leaves something to be desired, the qualitative results obtained with it are of considerable interest, as we shall now show.

B. DETERMINATION OF LIQUID JET FLOWFIELD

Detailed surveys were conducted in the $\bar{y}-\bar{z}$ plane at x ($\equiv \bar{x}/d_j$) = 50 for refrigerant-11 jets that were injected normally into an unheated (T_{t_∞} = 525°R), Mach 2.72 air-stream with p_∞ = 1 atmosphere, and two jet conditions: d_j = 0.027, p_{t_j} $\approx$ 905; and d_j = 0.052, p_{t_j} $\approx$ 302 (see Table 2, Tests 12 and 13). Since pressure and velocity gradients exist in the flow, significant differences can exist between composition distribution and the distribution of mass flux, which is a property of main interest.

- 30 -

Therefore, pitot and cone-static pressure surveys also
were made. Pitot and cone-static pressure data also
were measured for $d_j = 0.027$, $p_{t_j} \approx 211$ (Table 2, Test 11),
but complete mass-sampling data were not obtained for
this condition because it was established that a sizable
portion of the injectant occurred below $y = 4.6$ ($\bar{y} = 0.125$
inch), which was the minimum value at which data could
be measured because of the size of the probe. Limited
pitot-pressure data were measured at $x = 25$ for Test 13.

Vertical distributions of mass composition at five
lateral distances from the jet centerline are shown in
Fig. 14. Data could be measured only down to $y = 4.6$
and 2.3 in Tests 12 and 13, respectively. In general, the
data are rather well-behaved in regions where the injec-
tant mass content is less than $\sim 50\%$, but show more scat-
ter at higher compositions, which is not surprising in
view of the probe evaluation test results (Table 3) for
comparable conditions of stream temperature and compo-
sition level. Accordingly, the data curves drawn for the
high composition regions are open to question. This fact
will be examined later for the results shown in Fig. 14a
by comparing the injectant mass flow rates computed from
both the solid and dashed data curves drawn for $z = 0$,
2.5, and 5.0.

Some typical pitot and cone-static pressure data
are shown in Figs. 15 and 16 (the complete pressure data
for Tests 11-13 are given in the Appendix). These data
were measured with the probe rakes that were continuously
traversed in the lateral $(\bar{z})$ direction for various levels
above the plate surface $(\bar{y})$. The data were then cross-
plotted to obtain pressure distributions for various lateral
planes. The data for Test 13 were taken at more closely-
spaced vertical positions to obtain a more definitive mea-
sure of the flow structure that was shown to be needed on
the basis of results obtained in Tests 11 and 12. Of
particular interest are the pronounced pressure decreases
that occur in the jet region. It will be shown that this

(a)   TEST 12, $d_j = 0.027$ INCH, $p_{t_j} \approx 905$ PSIA, $M_\infty = 2.72$

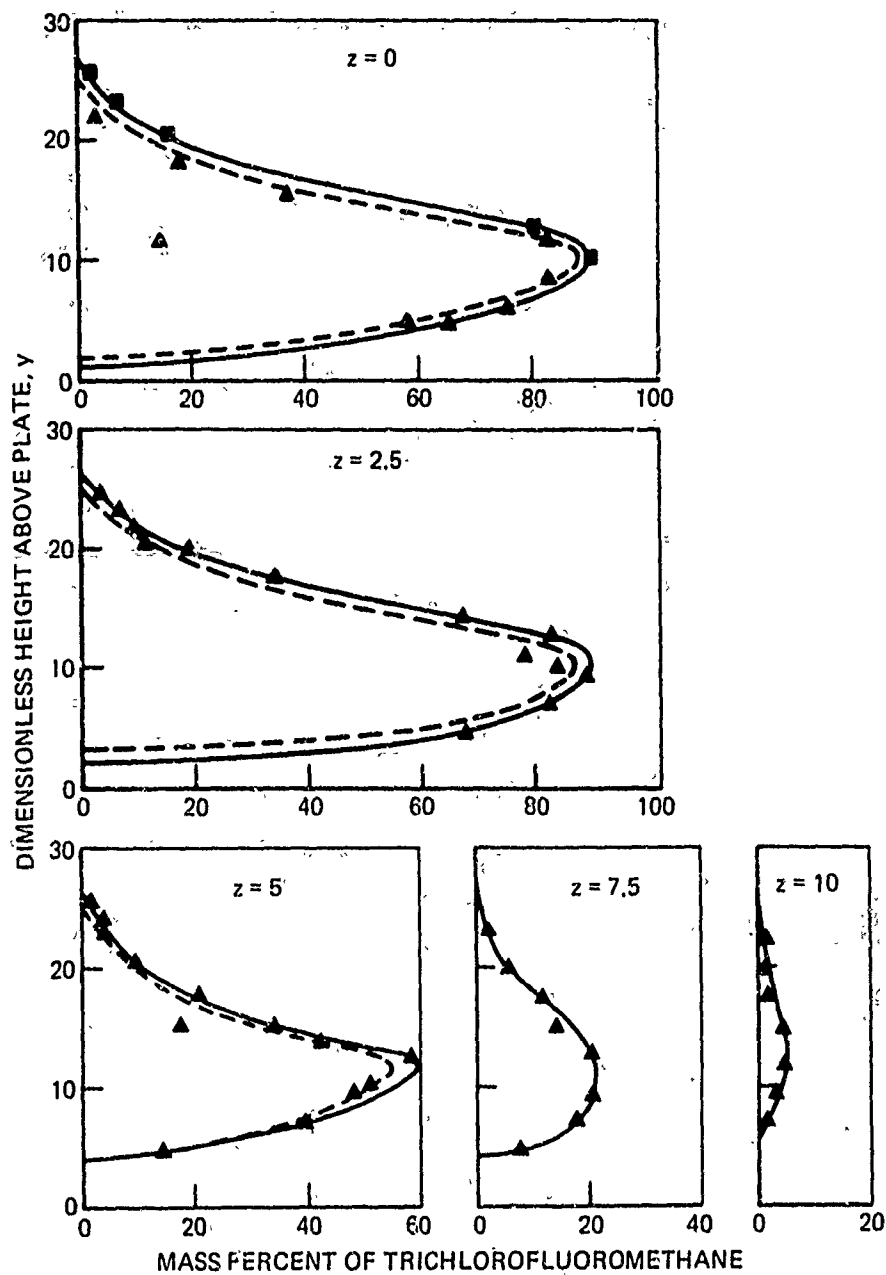FIGURE 14   MASS COMPOSITION DATA FOR LATERAL PLANE AT x = 50

- 32 -

(b) TEST 13, d_j = 0.052 INCH, p_{t_j} ≈ 302 PSIA, M_∞ = 2.72

DIMENSIONLESS HEIGHT ABOVE PLATE, y

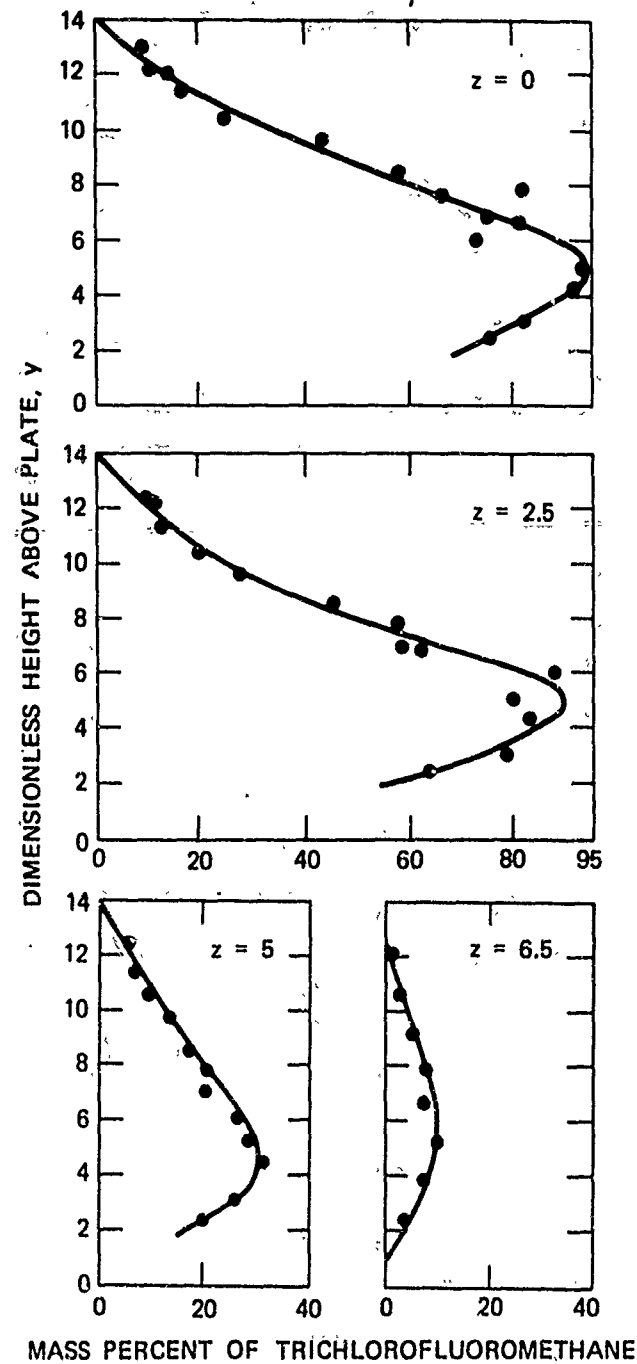MASS PERCENT OF TRICHLOROFLUOROMETHANE

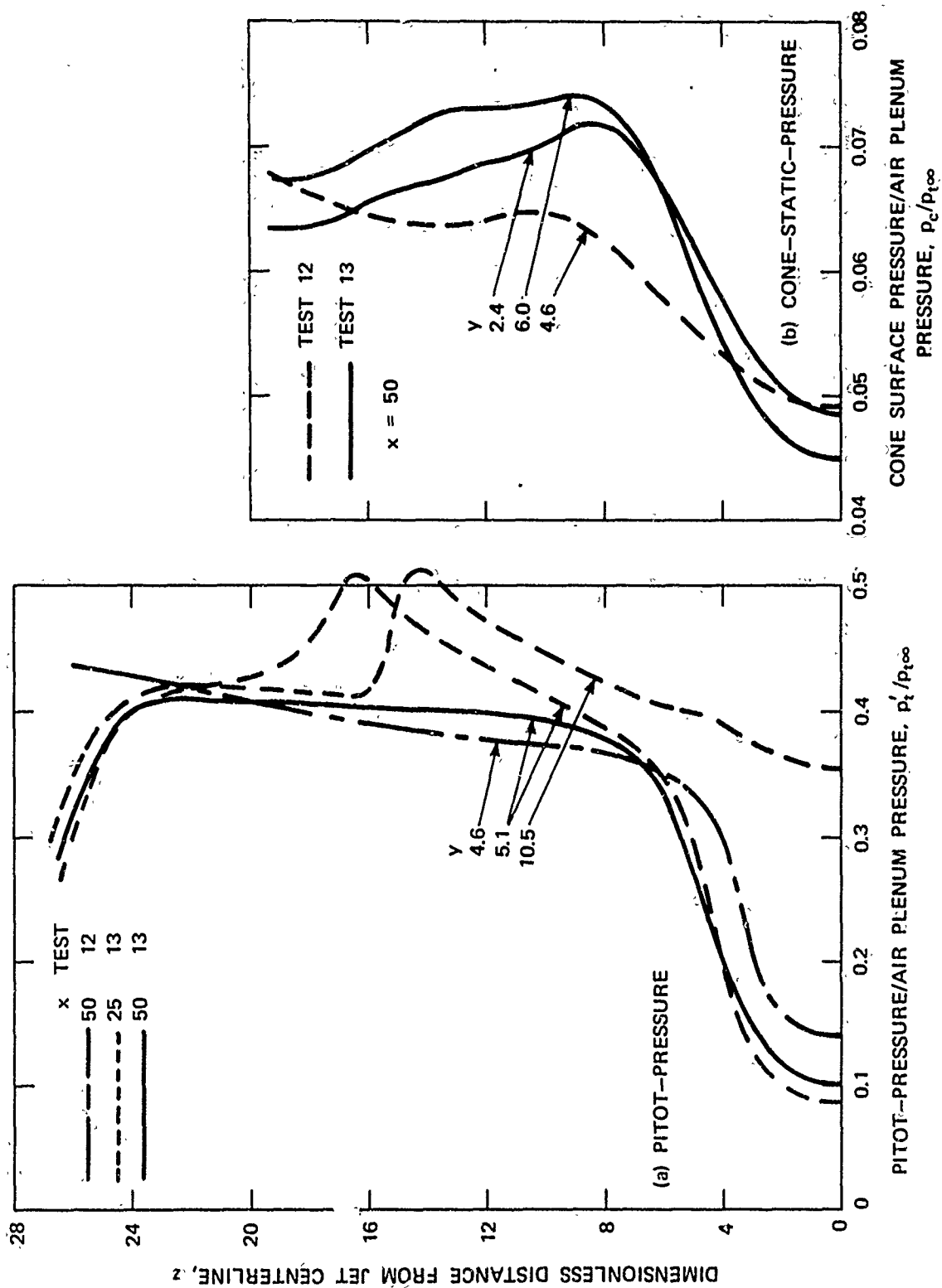FIGURE 14 (CONCLUDED)

- 33 -

FIGURE 15 TYPICAL PITOT-PRESSURE DISTRIBUTIONS FOR VARIOUS LEVELS
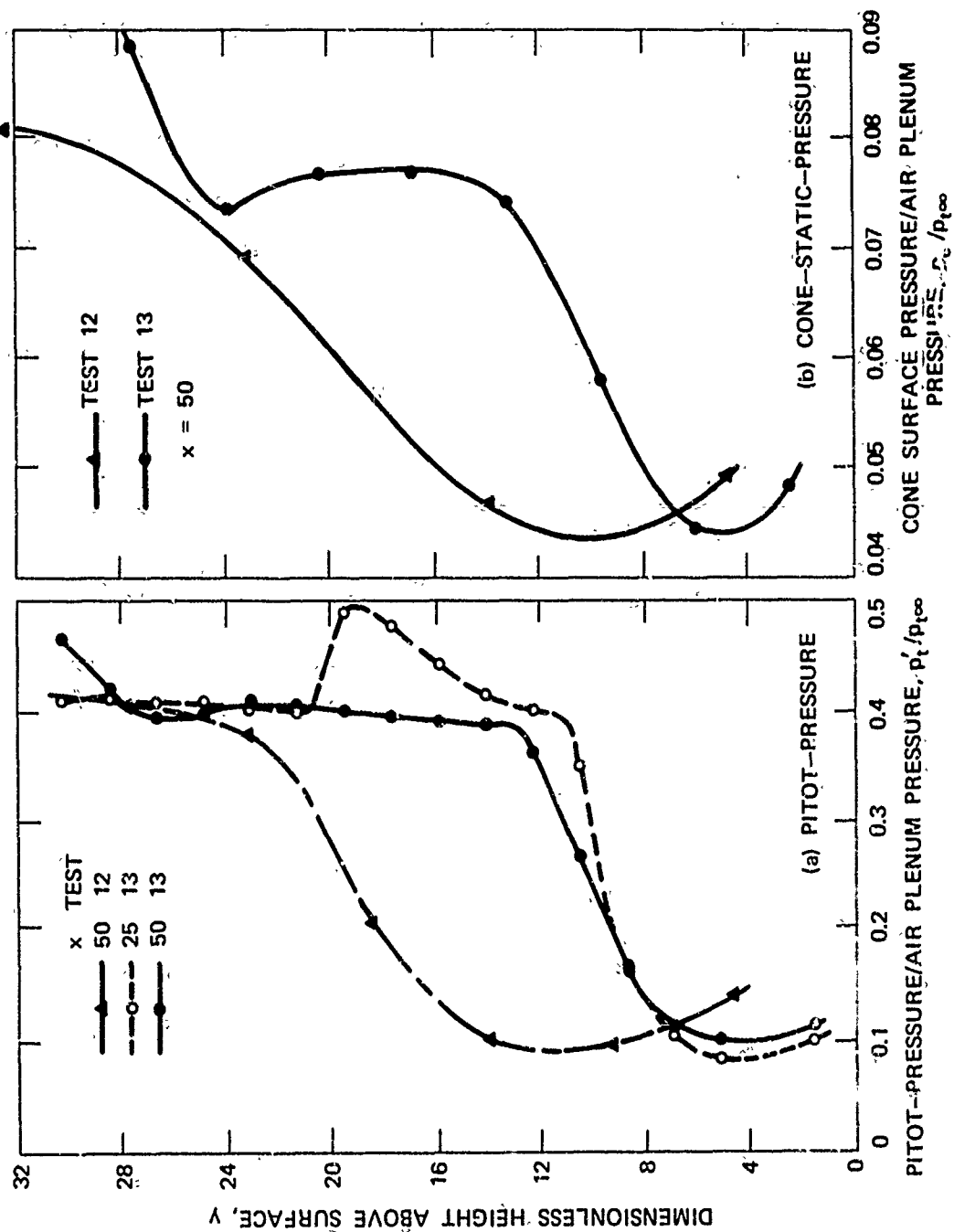ABOVE PLATE SURFACE

- 34 -

FIGURE 16   TYPICAL JET CENTERLINE PRESSURE DISTRIBUTIONS

- 35 -

feature of the pitot-pressure data, in particular, is useful for determining an approximate measure of the jet boundary geometry. The pitot-pressure maximum that occurs outside the jet structure, e. g. , at y = 19. 2 for x = 25 in Test 13 (Fig. 17a), is caused by the interaction bow shock, whose position corresponds to this maximum pressure. On the other hand, the interaction shock had already intersected the air jet boundary prior to x = 50 in Test 13, and the pitot-pressure decrease in the vicinity of z = 25 (Fig. 15a) occurs at the air jet boundary.

A difficult problem here is the need to specify local mixture quality and the local liquid-phase velocity, which may differ significantly from that of the gas phase. There also is a question of the extent to which the pressure measurements per se are affected by the liquid phase. For simplicity, the present data are reduced on the assumption that the gas flow properties can be measured independently of the presence of the liquid phase. Then, the gas flow properties are computed for either of two assumptions on mixture quality: the injectant is all gas or all liquid. The gas-phase stagnation temperature is taken in both cases to be that of the initial air plenum temperature, which was only slightly lower than that of the initial injectant plenum temperature. This last assumption is reasonable even for the case where the injectant is all vapor, because it is expected that the energy required to vaporize the liquid would have to be self-supplied and, hence, would decrease the overall temperature of the injectant.

With the foregoing assumptions, the gas flow properties are computed by the procedure detailed in the Appendix. The gas-phase static pressure and Mach number were deduced from the pitot-pressure and cone-static-pressure data by combining the Rayleigh pitot formula with solutions of the Taylor-Maccoll differential equation for supersonic flow around cones using the appropriate value of the specific heat ratio γ. In particular, $\gamma = 1.4$ was used for the case of no vaporization (all air),
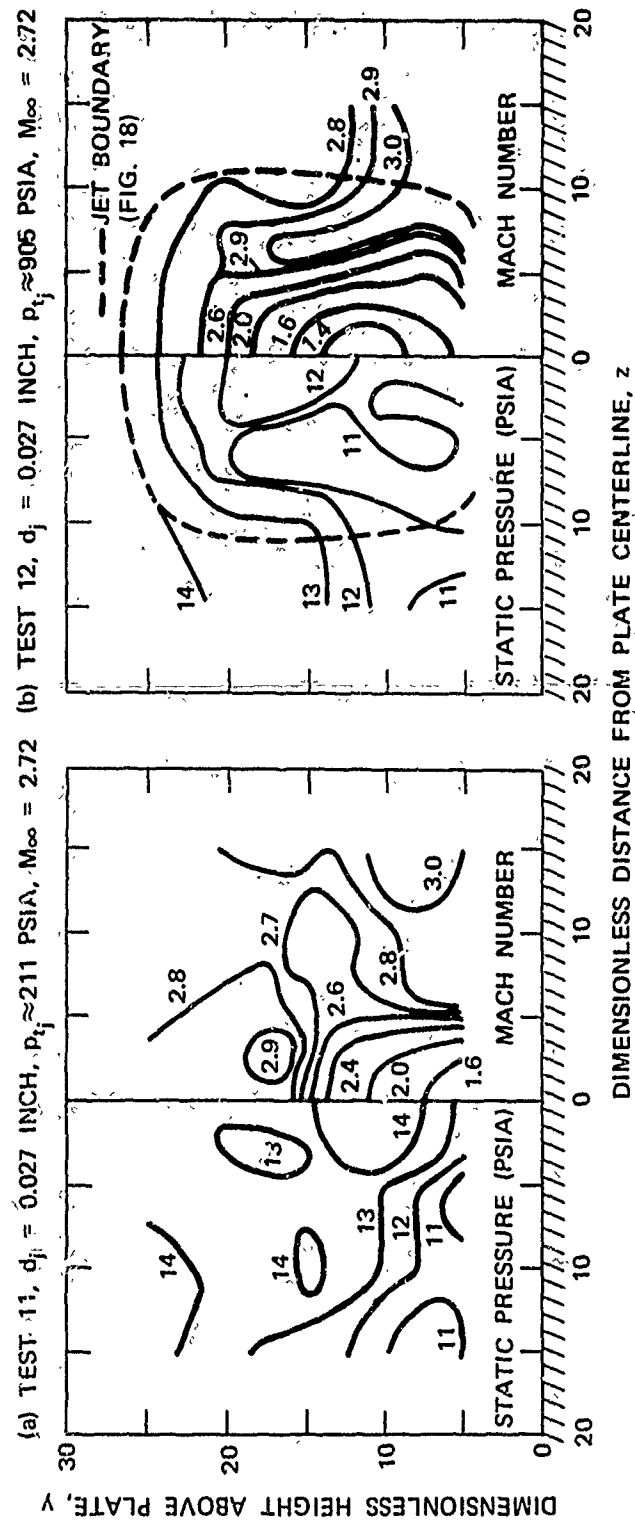
FIGURE 17 PRESSURE AND MACH NUMBER CONTOURS AT x = 50

(a) TEST 11, d_j = 0.027 INCH, $p_{t_j} \approx 211$ PSIA, M_∞ = 2.72   (b) TEST 12, d_j = 0.027 INCH, $p_{t_j} \approx 905$ PSIA, M_∞ = 2.72

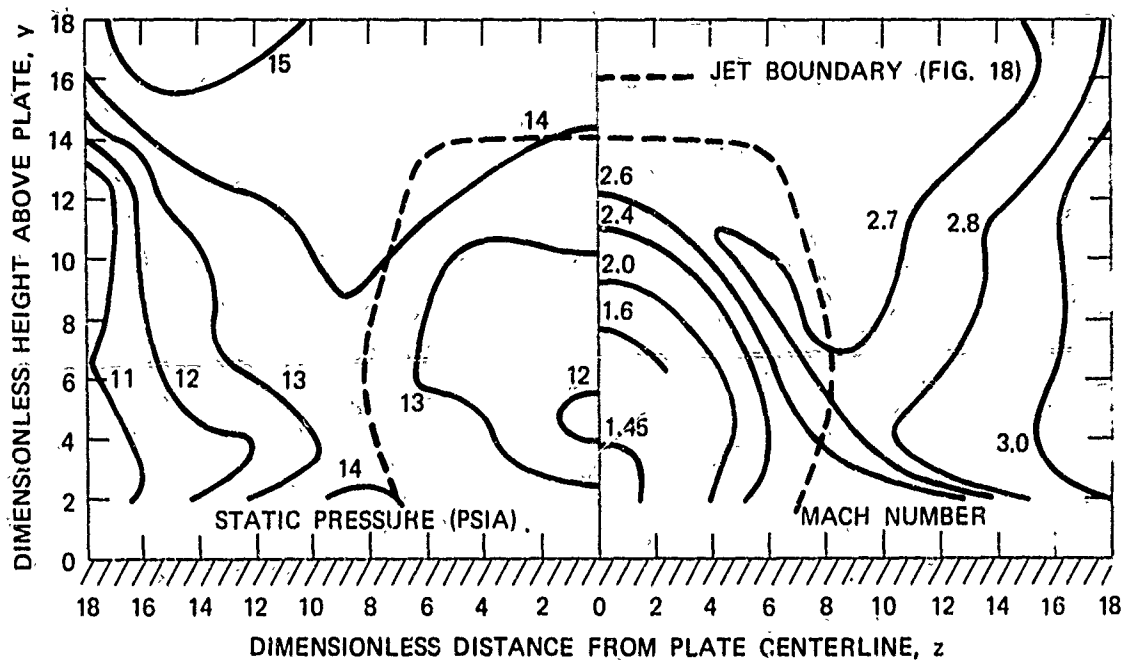(c)   TEST 13, d_j = 0.052 INCH, p_{t_j} ≈302 PSIA, M_∞ = 2.72

FIGURE 17   (CONCLUDED)

and γ was based on the local mixture composition for the case of complete vaporization. Similarly, the gas-phase molecular weight was based on either pure air or the local mixture composition. The adiabatic energy equation, the gas-phase equation of state, and the sound speed equation were then used to compute the local gas-phase mass flux, from which the local injectant mass flux was deduced. It is important to note that, so long as only the injectant mass flux is of interest, there is no need to specify the liquid-phase velocity in the case of no vaporization.

The pressure, Mach-number, and mass-flux distributions computed for the case of complete vaporization were cross-plotted to deduce the contours shown in Figs. 17 and 18. The results shown for the regions below y = 4.6 and 2.3 in Tests 12 and 13, respectively, are estimates. One means of judging the validity of these results is to compare the injectant mass-flow rates (w_j's) determined by integrating graphically the mass flux distributions with the metered input values (Table 4). When we consider the dashed curves shown for Test 12 in Fig. 14a, which favor the lower data points, the error in the integrated $\dot{w}_j$ is reduced from 58 to 34%; thus, the deduced flow rate is very sensitive to the interpretation of the composition data.

Table 4

Error in Integrated Mass Flux Compared to Metered $\dot{w}_j$

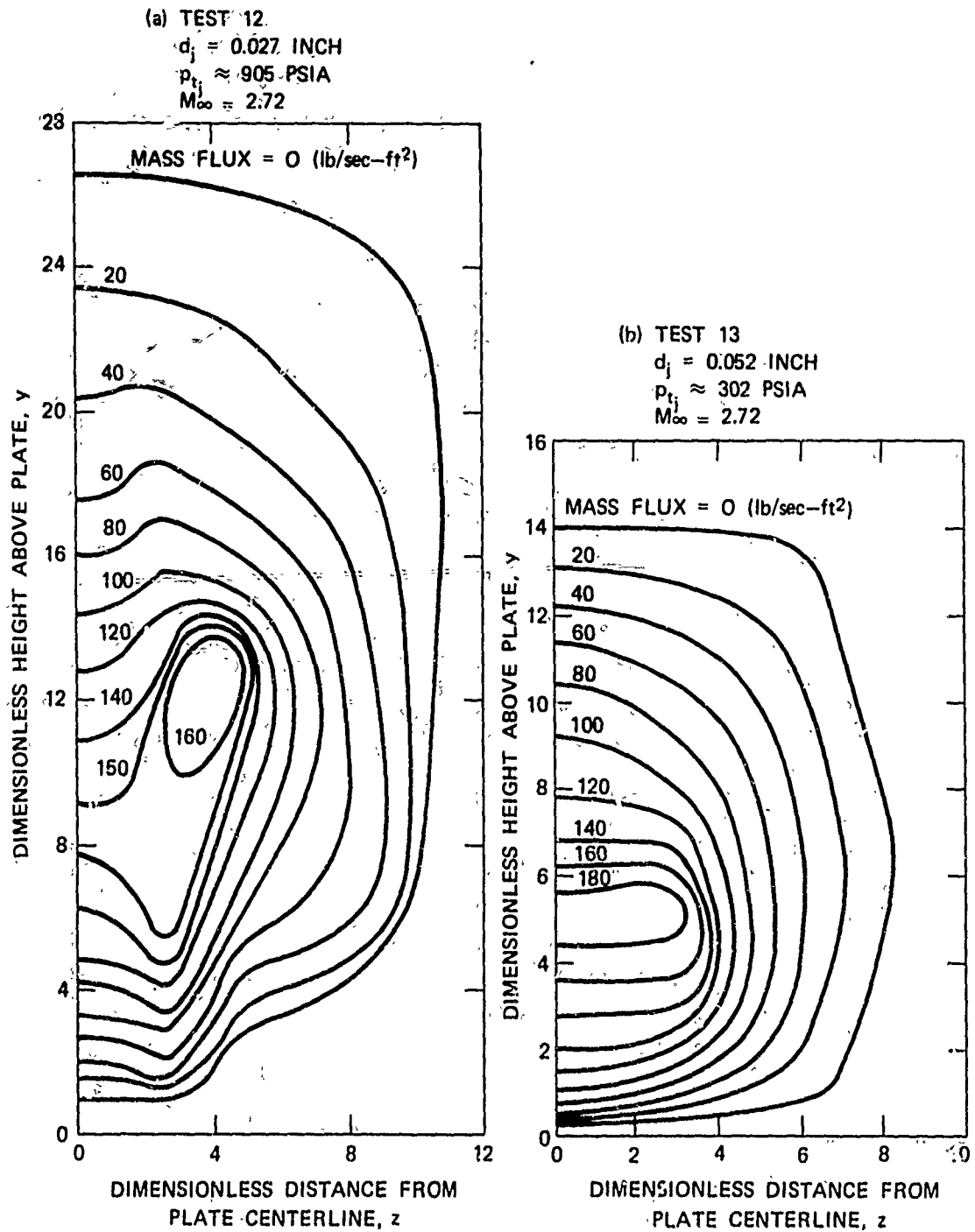| Measurement	Test 12		Test 13	
	$\dot{w}_j$(lb/s)	Error	$\dot{w}_j$(lb/s)	Error
Metered Input	0.099	--	0.199	--
Sampling (solid curves, Fig. 14)	0.156	+58%	0.255	+28%
Sampling (dashed curves, Fig. 14a)	0.133	+34%	--	--

FIGURE 18   MASS FLUX CONTOURS AT x = 50

When, for Test 12, the injectant is assumed to be all liquid, the deduced flow rate is about twice as large (~ 0.3 lb/s). Nevertheless, some portion of the injectant probably still was liquid at $x = 50$ in these tests, because both T_{t_j} and T_{t_∞} were below refrigerant-11's boiling temperature (535°R), and the local pressure was only slightly less than refrigerant-11's vapor pressure. The importance of knowing mixture quality is evident.

Nevertheless, we have assumed that the mass flux contours based on the all-vapor assumption (Fig. 18) are qualitatively useful and have used them to derive spatial distributions of the injectant. Figure 19 shows that for Tests 12 and 13, respectively, 66 and 70% of the mass is found below the half-height of the jet, and 75 and °5% of it lies within the half-width (i.e., the central 50%) of the jet. These results are very significant for scramjet engine design. In addition, for Test 12, the mass percentage curve peaks in a lateral plane ≈ 3 jet diameters from the centerline. This observation is consistent with the previously described photographic data for jet spreading that showed mass apparently being stripped from the periphery of the jet. The failure to find an off-axis maximum for the $d_j = 0.052$ results of Test 13 can be explained by the fact that, if such a maximum existed, it could have been removed by the mass diffusion and mixing processes, which would have been operative for a longer period of time (by about a factor of 2, since $\bar{x}$ was twice as great) in this test.

The value of the present results would be enhanced if the mass distribution curves were found to be similar on some dimensionless basis. This possibility is examined in Fig. 20, where the local jet height $\bar{y}_B$ and width $\bar{z}_B$ have been used to nondimensionalize distance. Because of the varying degree of error that is known to exist in the mass flux data, it is not expected that the distributions from the two tests in either $\bar{y}$ or $\bar{z}$ would reduce to a single curve. Nevertheless, they are fairly
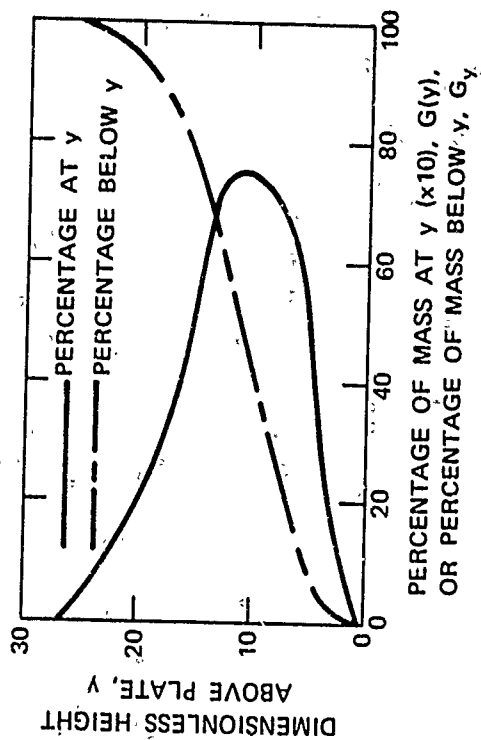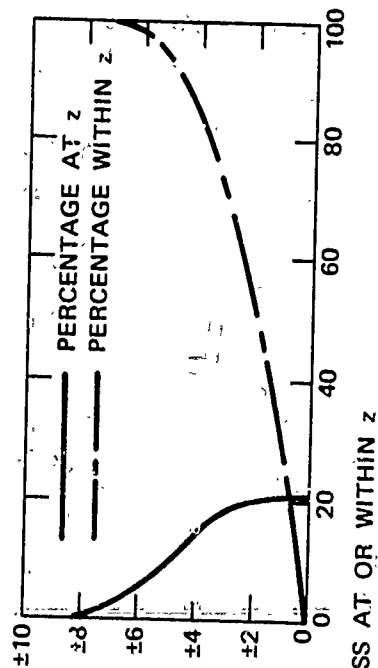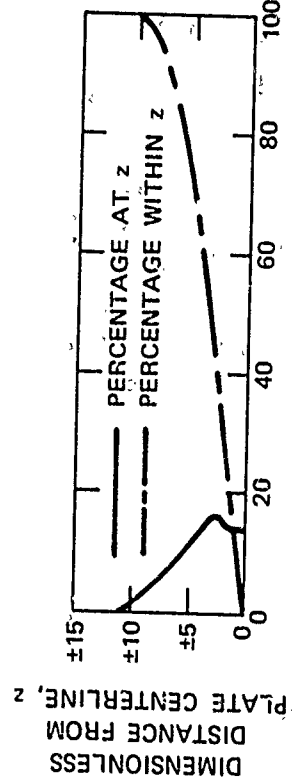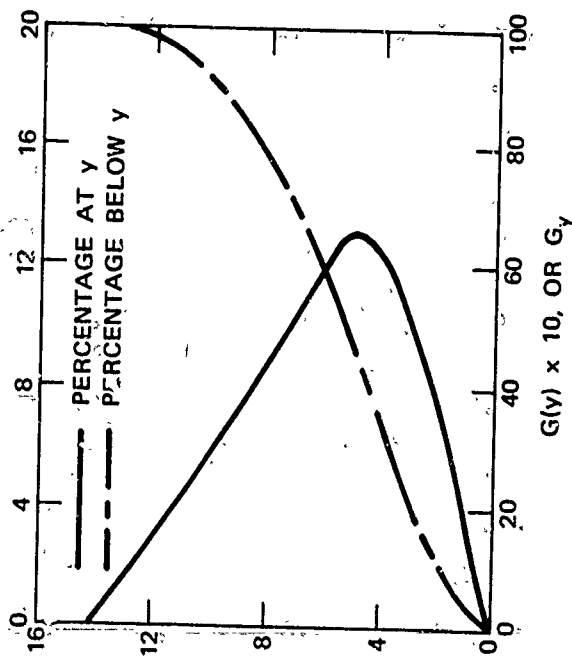
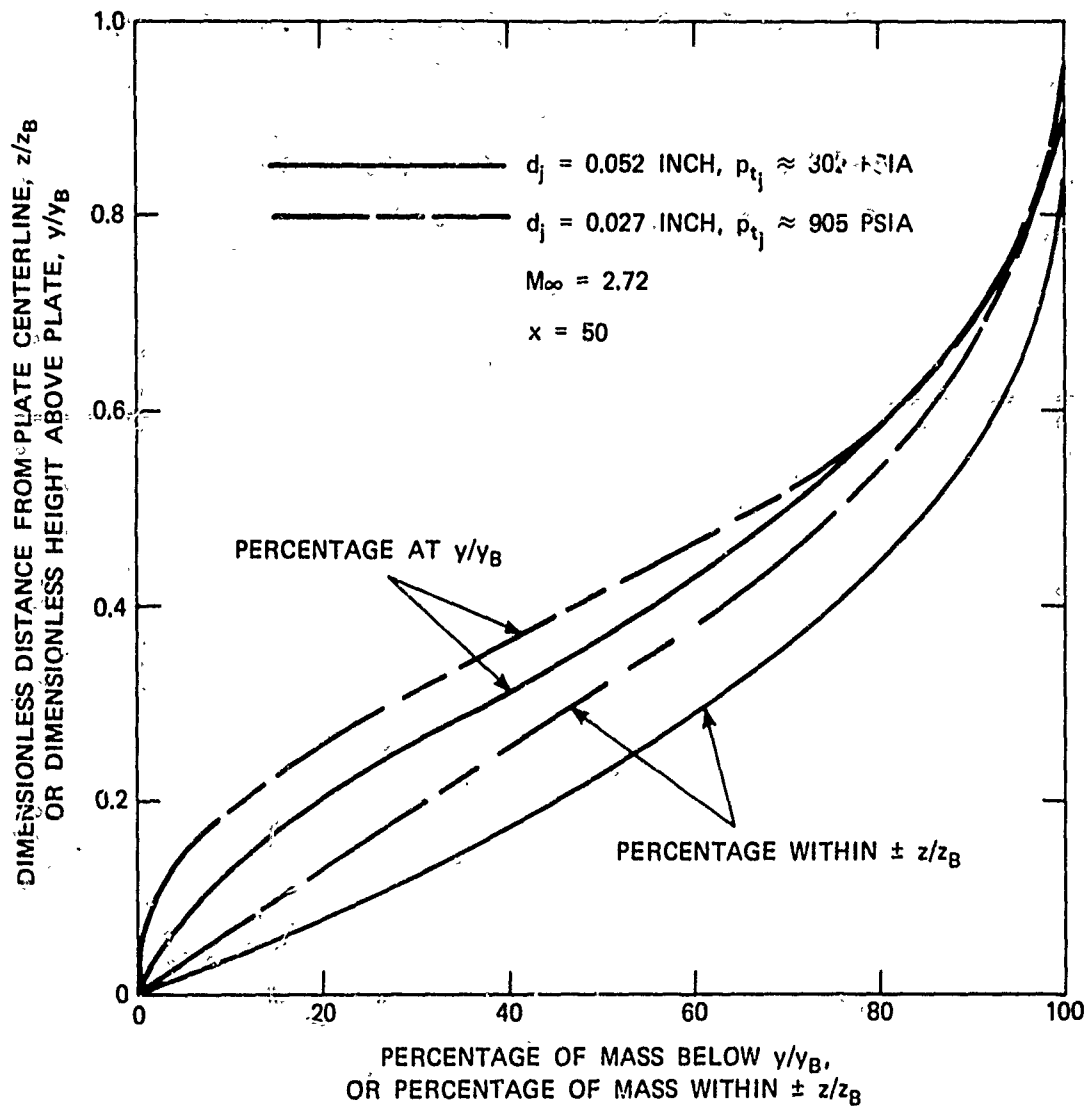FIGURE 19   DISTRIBUTION OF INJECTANT MASS AT x =50

- 42 -

FIGURE 20   SIMILARITY OF DIMENSIONLESS INJECTANT MASS DISTRIBUTIONS

- 43 -

similar, even though the $\bar{x}$'s differed by a factor near 2. This result suggests that, in the absence of further data, these curves can be used to estimate mass distributions for other conditions, using the empirical Eqs. (1) and (10) to determine $\bar{y}_B$ and $\bar{z}_B$.

In this respect, it is of interest to examine the extent to which the mass-sampling results of Fig. 18 agree with Eqs. (1) and (10), which were derived from the photographic results (Table 5). It is recalled that Eq. (10) refers to the maximum width, which is assumed to occur by $x \approx 150$, whereas the data are for $x = 50$. However, it is estimated from the photographic data (e. g., the $M_\infty = 2.72$ results in Fig. 10) that z_B increases by less than 10% in going from $x = 50$ to $x = 150$. Referring to Table 5, we see that the empirical equations predict y_B's and z_B's that are, respectively, 16-19% and 19-21% lower than those (at the 0% level) from the sampling data. It must be considered, however, that injectant fluid near the jet boundary occurs in the form of a low-concentration vapor and/or extremely small droplets and, hence, would not be detected in a photograph. Therefore, it is reasonable to use a finite composition level in making our comparison.

Table 5

Comparison of Jet Boundary Locations

Basis	Test 12		Test 13	
	y_B	z_B	y_B	z_B
Empirical Formulas	21. Ω	17. 6[+]	11. 8	13. 0[+]
Mass Fraction Data (0% level)	26. 5	21. 6	14. 1	16. 5
Mass Fraction Data (10% level)	21. 7	17. 6	12. 5	13. 1
Mass Distribution (95% of mass)	20. 6	16. 4	10. 9	10. 8
Pitot-Pressure Data	22. 8	17. 6	13. 1	14. 9

[+]Maximum jet width — assumed to occur by $x \approx 150$

- 44 -

If the 10-mass-percent level is arbitrarily chosen, the y_B's and z_B's agree well. Another means of evaluating the usefulness of the empirical predictions is to consider the amount of mass for which they account. If we determine from the dash-dot curves in Fig. 19 the y and z values that account for 95% of the injectant mass, we find that they are lower than the empirically predicted y_B and z_B. Hence, we conclude that the empirical predictions are reasonably accurate, accounting for $\sim$ 96% of the injectant mass.

Pitot-pressure data also are useful for a rough determination of the jet boundary geometry, as shown in Table ˮ which includes y_B and z_B values at x = 50 estimated ι jet boundary contours (solid curves in Fig. 21) define. loci of points at which the knee of the pitot-pressure distribution (in the y- or z-direction) occurs; i.e., points at which the pitot-pressure, as it increases above its minimum value (which occurs in the region of maximum injectant composition), reaches the nearly constant level that exists between the jet boundary and the interaction shock. Referring to Fig. 15, one sees that there is some arbitrariness in defining the knee of a pitot pressure curve. Nevertheless, the jet boundaries so determined are in better agreement with the mass-sampling data (0% level) than are the results from the empirical equations, as shown in Table 5. Figure 21 also includes a jet boundary contour based on pitot-pressure data at x = 25 for Test 13 (dash-dot curve), and it is noted that the pressure data show a 16% increase in y_B in going from x = 25 to x = 50, whereas Eq. (1) predicts a 12% increase.
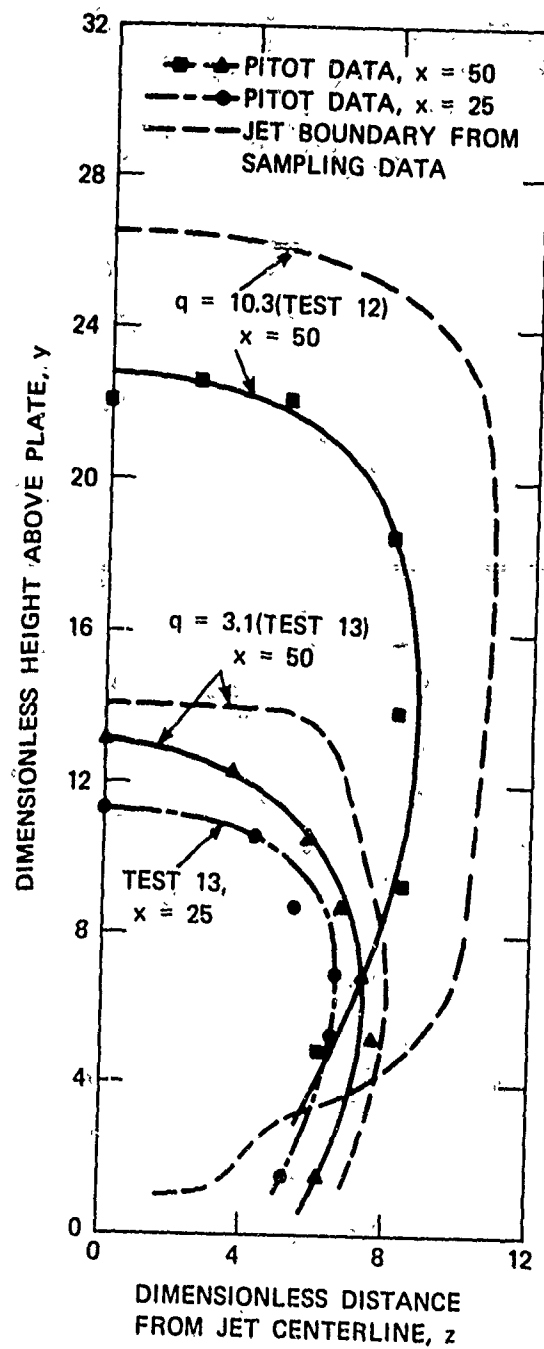
FIGURE 21   APPROXIMATE JET BOUNDARIES DEDUCED
FROM PITOT-PRESSURE DATA

- 46 -

SECTION V

THEORETICAL STUDIES OF JET PENETRATION

A. GENERAL FEATURES OF FLOW MODEL

The usual procedure for predicting the trajectory of a liquid jet element of infinitesimal length $d\bar{s}$ and mass m (Fig. 22) is to apply the normal component of the momentum equation to obtain:

$$F_n = - mV_j^2/R = - \rho_j \bar{A} d\bar{s} \, V_j^2 \, d\alpha/d\bar{s} , \qquad (11)$$

where $R = d\bar{s}/d\alpha$ is the local radius of curvature of the trajectory, and ρ_j and the magnitude of V_j are assumed constant at their initial values. The advantage of using local-coordinates $\vec{n}$, $\vec{s}$ is that Eq. (11) holds for either constant or varying m, when the velocity of the element is always along $\vec{s}$. Neglecting the relatively small gravity force, the force F_n can be represented by:

$$F_n = C_D \, \bar{q}_\infty \sin^2\alpha \, \bar{w} d\bar{s} , \qquad (12)$$

where C_D is the local drag coefficient of an element in a crossflow ($\alpha = 90°$). Equations (11) and (12) are combined to give, after introducing dimensionless quantities ($A \equiv \bar{A}/\bar{A}_j$; $q \equiv \bar{q}_j/\bar{q}_\infty$; $s \equiv \bar{s}/d_j$; $w = \bar{w}/d_j$),

$$(w/A) \, ds = - (\pi q/2C_D) \, d\alpha/\sin^2\alpha . \qquad (13)$$

To proceed, it is necessary to specify local values (as functions of s or α) of w, A, and C_D, which are all functions of jet distortion and disintegration and are strongly interrelated. When this is done, Eq. (13) and the relations dx = ds cos α and dy = ds sin α are used to determine
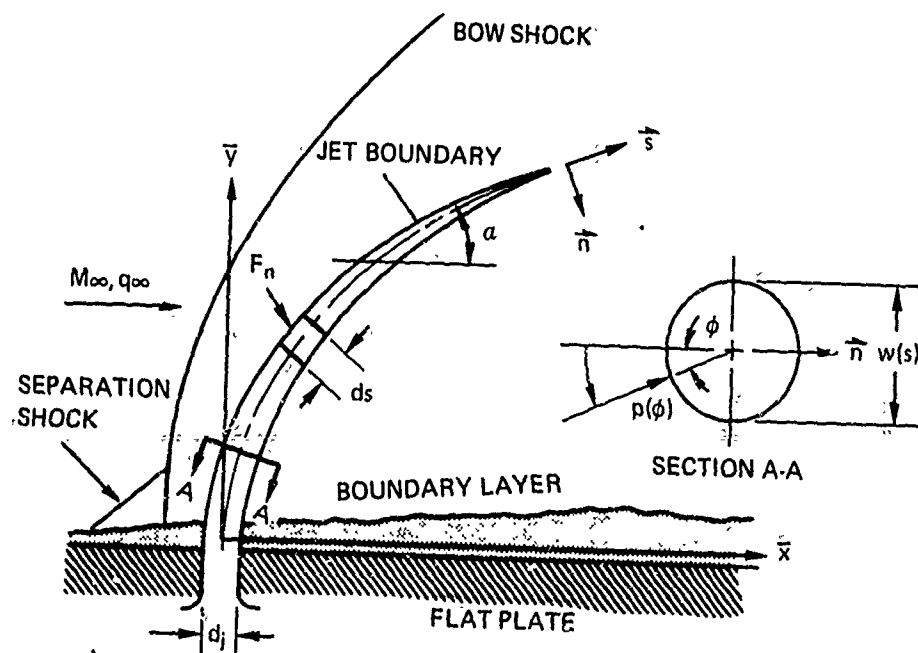
FIGURE 22 SCHEMATIC REPRESENTATION OF LIQUID INJECTION INTO SUPERSONIC STREAM

the centerline trajectory in the x, y plane. (In general, it is necessary first to determine $s = s(\alpha)$ before these relations can be applied.)

Although the cross-sectional shape of the liquid element probably is noncircular, C_D is often taken to correspond to the drag on a right circular cylinder and is then based on either theory or experiment. An example of the former approach is the Newtonian drag theory, in which local pressure on the forward portion of the cylinder is computed by assuming that particles striking the surface lose their surface-normal component of momentum. The pressure distribution around the body is then found to be:

$$\text{For} \quad -\pi/2 \leq \varphi \leq \pi/2, \quad C_p = C_{p_0} \cos^2 \varphi \, ,$$

$$\text{For} \quad \pi/2 < \varphi < -\pi/2, \quad C_p = 0 \, . \tag{14}$$

For an inclined cylinder ($\alpha \neq 90°$), only the component of the freestream flow that is normal to the cylinder axis contributes to the drag, in which case $C_p \equiv (p - p_e)/\overline{q}_e \sin^2\alpha$. A second expression for the force F_n is now determined to be:

$$F_n = 2 \int_0^\pi p \cos \varphi \, (\overline{w}/2) \, d\varphi \, d\overline{s} \, ,$$

$$= (2/3) \, \overline{w} d\overline{s} \, C_{p_0} \, \overline{q}_\infty \sin^2\alpha \, . \tag{15}$$

Combining Eqs. (12) and (15), we find:

$$C_D = (2/3) \, C_{p_0} \, . \tag{16}$$

Here C_{p_0} is the stagnation-point ($\varphi = 0$) pressure coefficient. In "regular" Newtonian theory, $C_{p_0} = 2$, but a

constant value for C_{p_0} is incorrect for compressible flows. Thus, in the "modified" Newtonian theory, C_{p_0} is based on the actual stagnation pressure that can generally be calculated as a function of M_∞. For subsonic flow, the isentropic flow relationships give:

$$C_{p_0} = (2/\gamma M_\infty^2) \left\{ [1 + (\gamma - 1) M_\infty^2/2]^{\gamma/(\gamma-1)} - 1 \right\} . \qquad (17)$$

For supersonic flow, the normal-shock relationships give:

$$C_{p_0} = (2/\gamma M_\infty^2) \left\{ [(\gamma + 1)/(2\gamma M_\infty^2 - \gamma + 1)]^{1/(\gamma-1)} [(\gamma + 1) M_\infty^2/2]^{\gamma/(\gamma-1)} - 1 \right\} . \qquad (18)$$

When Eqs. (17) and (18) are applied to an inclined cylinder, M_∞ should be replaced by $M_\infty \sin \alpha$, so that, rigorously, $C_{p_0} = C_{p_0} (M_\infty, \alpha)$ should be used in integrating Eq. (13).

Variation of the Newtonian C_D with M_∞ is compared with experimental data for a solid, normal ($\alpha = 90°$), constant-area cylinder (Ref. 15) in Fig. 23 (the approximation shown there is discussed later). The difference between data and theory is generally sizable, except for the hypersonic regime ($M_\infty \gtrsim 5$), where the agreement between data and the modified theory is very good. The deviation at lower M_∞'s reflects viscous and base-drag effects that occur in the real situation. However, none of the curves necessarily applies to a liquid jet, since jet disintegration and distortion could lead to viscous and base-drag effects that differ significantly from those occurring on a solid body. Moreover, the application of C_D for a right cylinder to a curvilinear deflected jet incorrectly implies an equality between bow shock and jet centerline shapes. Hence, it is concluded that no really satisfactory basis exists for predicting the drag on a liquid jet.
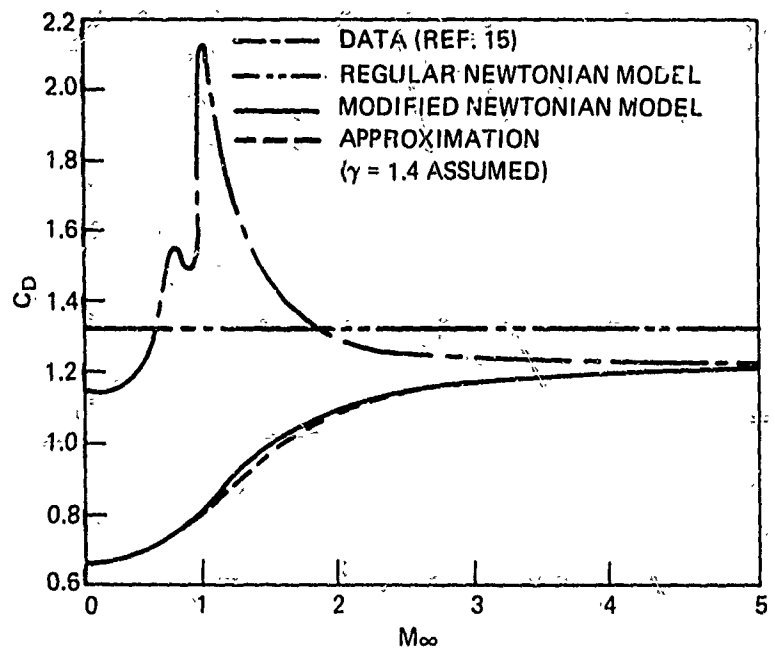
FIGURE 23   DRAG COEFFICIENT FOR RIGHT CIRCULAR CYLINDER

The situation with regard to predicting jet disintegration and distortion is even less satisfactory. One of the more comprehensive studies in this area was made by Clark (Ref. 16), who determined the change in normalized jet cross-sectional area, $A \equiv \overline{A}/A_j$, by measuring the electrical resistance variation along the length of a water jet (V_j = 65 to 430 ft/s) in a nitrogen crossflow (V_∞ = 15 to 155 ft/s), from which he derived:

For $\epsilon < 1$, $A = 1$;

For $\epsilon \geq 1$, $A = [0.00392 (7.68 \epsilon - 1)(\epsilon -1)^{2.34} + 1]^{-1}$,   (19)

where $\epsilon = [1 + (V_j/V_\infty)^2] s^2/q$ is called the breakup parameter. The occurrence of ϵ as an independent variable results from a simple theoretical model of jet breakup at high Weber numbers in which it is assumed that jet breakup is controlled by the rate at which the jet spreads transversely to the oncoming stream. The spreading is assumed to be effected only by the dynamic forces imposed by the gas stream and the inertial forces within the jet. In fact, Clark reasoned that jet width should vary as follows:

$$w = (1 + 2\epsilon) .$$ (20)

Clark's data and the correlation given in Eq. (19) are shown in Fig. 24. While considerable scatter (up to ±25%) exists in data, their uniqueness makes them important and useful.

Before proceeding, it is important to note that, in formulating the flow model as presented here, the separation region that is experimentally observed to exist in the vicinity of the orifice exit (see Fig. 22) is neglected. Hence, it is to be expected that analyses based on the above formulation will predict an incorrectly low penetration for the initial portion of the jet trajectory, independently
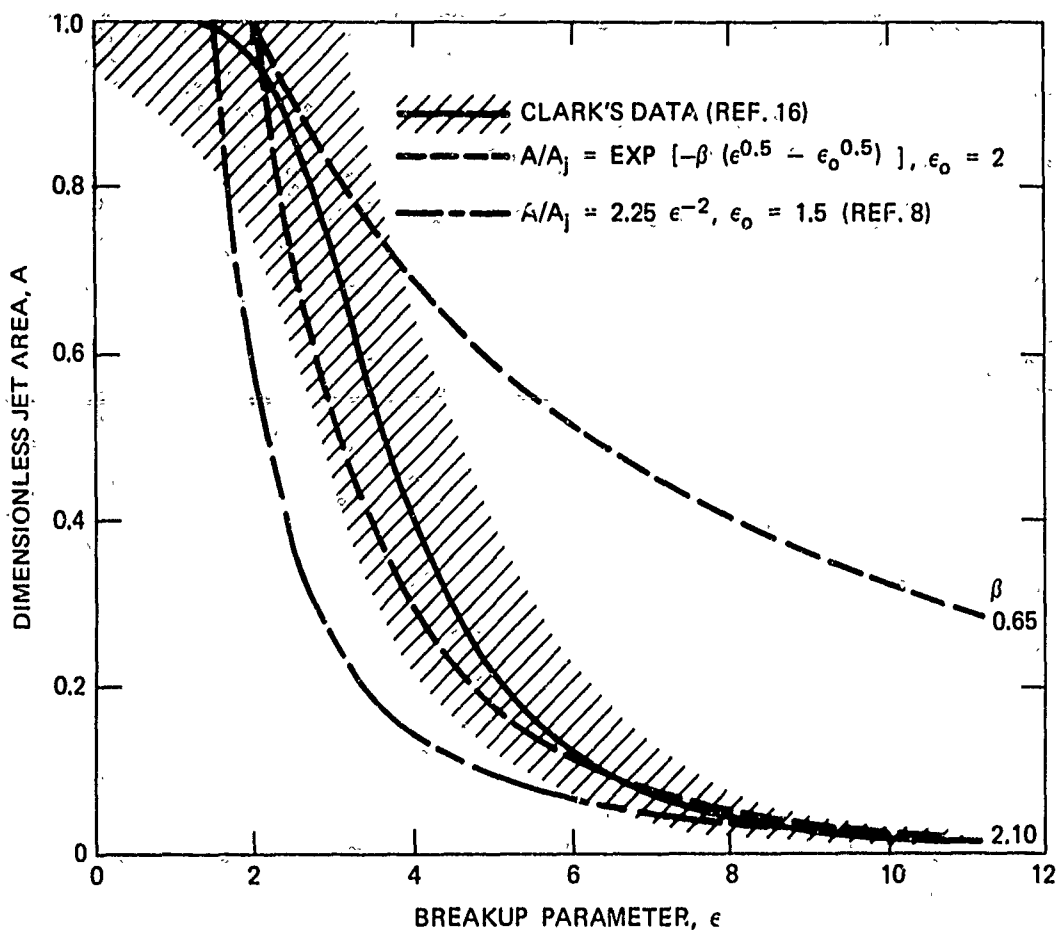
FIGURE 24   JET BREAKUP AS A FUNCTION OF BREAKUP PARAMETER

- 53 -

of other assumptions made in a particular analysis. In fact, this will be found to occur for those analyses discussed in this report.

B. REVIEW OF EXISTING ANALYSES

The studies of Forde, et al. (Ref. 6) and Catton, et al. (Ref. 8) present two approaches to the theoretical prediction of jet penetration that are fairly representative of the scope of existing analyses. In both analyses, centerline trajectory equations are derived for arbitrary injection angles which, when specialized to normal injection, can be expressed as follows ($d_e = d_j$ is assumed):

$$y_c = K_1 y_0 + K_2 \, \ell n \left(K_3 + (x - x_0)/K_2 + \left\{ [K_3 + (x - x_0)/K_2]^2 - 1 \right\}^{0.5} \right), \quad (21)$$

where $K_1 \equiv (K_4 - K_2)/K_4$, $K_3 \equiv (x_0 + K_4)/K_4$, and where K_2, K_4, x_0, and y_0 are constants that depend upon the assumed models for jet cross-sectional distortion, disintegration, and drag (x_0 and y_0 actually define the initial centerline location; however, they may be multivalued for a given trajectory if the integration of Eq. (13) is done piecewise because of changes in the functional form of w, A, or C_D). To assess the analyses of Refs. 6 and 8, we shall compare their predictions of jet centerline penetration with the empirical correlation of jet boundary penetration given in Eq. (1). (The comparison is reasonable, since in the theoretical models, the difference between centerline and boundary locations is small — half the local jet thickness in the $\vec{n}$ - direction.) Observing that Eq. (21) generally does not predict $y_c \propto q^{0.5}$, we shall compare the equation with Eq. (1) for a range of q.

In Ref. 6, jet disintegration and cross-sectional deformation are neglected, and the jet is assumed to be a constant-diameter cylindrical body; hence, $w/A = 1$, $x_0 = y_0 = 0$, and $K_4 = K_2 = \pi q/2 C_D$. In addition, it is assumed that $C_D = C_D (\gamma, M_\infty) \neq C_D (\alpha)$, where C_D is based on the

- 54 -

Newtonian theory. Hence, C_D is either 1.33 for regular Newtonian theory or ≤ 1.23 ($M_\infty \rightarrow \infty$) for the modified Newtonian theory with $\gamma = 1.4$. The prediction for $C_D = 1.23$ is compared with Eq. (1) for q = 3, 30, and 100 in Fig. 25, where it may be seen that for $q \geq 3$, the predicted penetration exceeds the data for $x \geq 35$. Increasing C_D to 1.33 does not noticeably improve the agreement. In fact, a C_D as high as 2.13 (the maximum experimental value shown in Fig. 23) is required to obtain only fair agreement over the range of q tested.

The analysis of Ref. 8 incorporates experimentally measured effects of jet distortion and disintegration. They use the data of Clark (Ref. 16) as a guide in deriving an expression for local jet area A; in particular, they assume that $A = 1$ up to a point s_0, beyond which $A = 2.25 \, q^2 s^{-4}$; hence, $s_0 = (1.5q)^{0.5}$. The foregoing expressions are compared to Clark's data in Fig. 24. To account for jet deformation, w is assumed to reach a maximum value of 1.6 at s_0, beyond which $w = e \, q^f s^{-g}$, where e, f, and g are constants. They arbitrarily assume g to be 4, which makes w/A independent of s and simplifies the integration of Eq. (13). They use e = 1, and f = 1.25, to give the best fit between their predicted and measured trajectories. (Actually, their choices for various constants appearing in the analysis result in some inconsistencies; for example, the values chosen for e and f do not give $w = 1.6$ at $s = s_0$.) The net result of these various assumptions is to divide the trajectory into two regions, in both of which the jet is, effectively, a constant-diameter cylinder. In the first region, $x_0 = y_0 = 0$, and $K_4 = K_2 = \pi q/2C_D$, as in Ref. 6, while in the second region (which starts at the following values of x_0, y_0):

$$x_0 = (K_4^2 + 1.63 \, q^{1.24})^{0.5} - K_4 \, ,$$

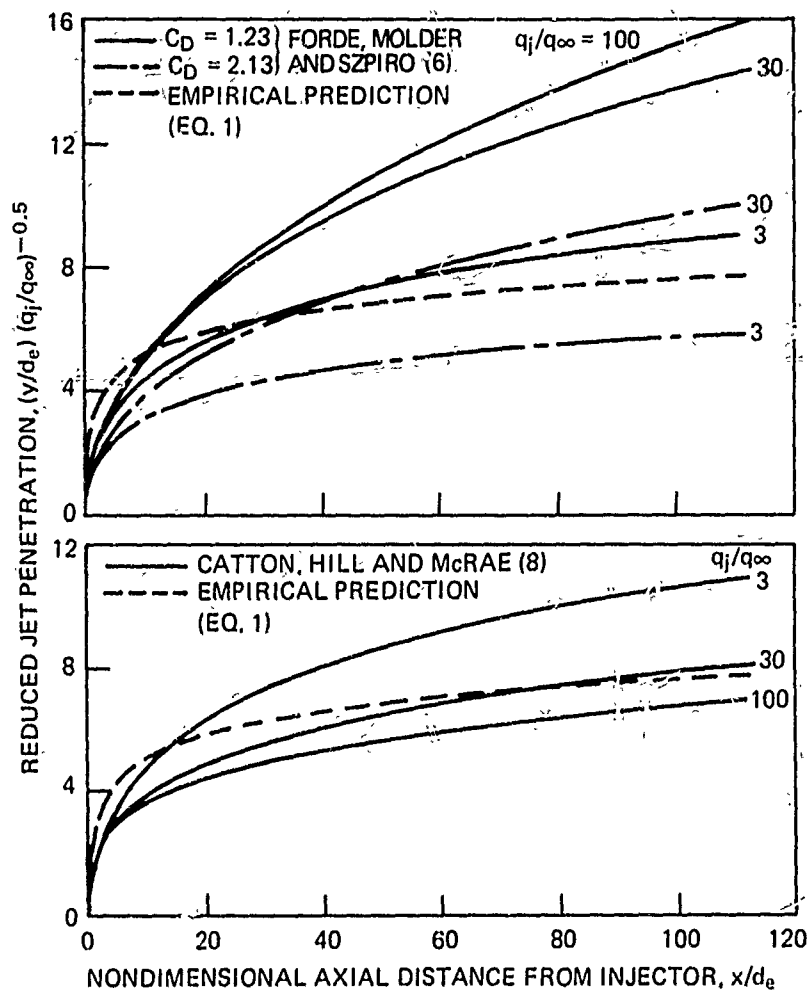$$y_0 = K_4 \, \ell n \left\{ 1 + x_0/K_4 + [(x_0/K_4)^2 + 2x_0/K_4]^{0.5} \right\} \, ,$$

FIGURE 25   COMPARISONS OF EXISTING THEORETICAL PREDICTIONS
TO PRESENT DATA

and $K_2 = (1.32\pi/C_D) \, q^{0.385}$. In both regions, C_D is based on the modified Newtonian theory corresponding to hypersonic ($M_\infty \to \infty$) flow. In particular, they use $C_D = (2/3)(\gamma + 3)/(\gamma + 1)$, or $C_D = 1.22$ for $\gamma = 1.4$. In effect, this model increases (when $q \geq 4.9$) the drag in the second region by the factor $0.38 \, q^{0.62}$. Figure 25 shows that the model agrees fairly well with experiment for $q \gtrsim 30$, but agreement is poor for $q \simeq 3$. Observe that this model gives a smaller dependency of the reduced penetration on q and that the dependency is reversed from that predicted by the analysis of Ref. 6. For the same level of C_D ($C_D \approx 1.2$), the penetration predicted by this model is considerably improved over that predicted in Ref. 6, a fact that is presumably due to the inclusion of jet disintegration effects.

C. PRESENT ANALYSIS

The theoretical studies considered in the previous section have shown the importance of including jet disintegration effects in the flow modeling. While this was done in Ref. 8, the amount of empiricism introduced into that analysis limits the versatility of the results to an extent that makes it difficult to classify and assess the effects of various assumptions. Therefore, the analysis does not permit optimum use of experimental data to suggest further improvements in the theoretical model. Moreover, it does not permit computation of the injectant mass distribution. Accordingly, a new theoretical analysis was developed for predicting the centerline trajectory of a normally injected, disintegrating liquid jet, such that the effects of varying jet breakup rate, M_∞, and C_D can be assessed by comparing the predicted injectant mass distribution with experimental data.

In the present analysis, Clark's (Ref. 16) experimental data (Fig. 24) were fit with the following expression for local jet area:

For $0 \leq \epsilon \leq \epsilon_0$, $A = 1$.

$$\text{For } \epsilon > \epsilon_0, \quad A = \exp\left[-\beta(\epsilon^{0.5} - \epsilon_0^{0.5})\right]. \tag{22}$$

- 57 -

For liquid injection into supersonic flow, $V_j/V_\infty \ll 1$, so that $[1 + (V_j/V_\infty)^2] \approx 1$, $\epsilon \approx s^2/q$, which is assumed hereafter. Figure 24 shows that with $\epsilon_0 = 2$ and $\beta = 2.1$, Eq. (22) falls within the region of certainty of the data. An advantage of the form of Eq. (22) is that, for conditions assumed in this analysis, the momentum equation (Eq. (13)) can be integrated in closed form. Moreover, Eq. (22) does imply a physically reasonable description of jet breakup that is shown by its differentiation:

$$\frac{dA}{ds} = -\frac{\beta}{q^{0.5}} A \equiv -\beta \frac{q_\infty^{0.5}}{q_j^{0.5}} A , \qquad (23)$$

i.e., following the jet path, the local disintegration rate is proportional to local jet cross-sectional area, increases with the square root of the freestream dynamic pressure and decreases with the square root of the jet dynamic pressure. However, it will be shown later that ϵ_0 and β may vary with q, so that the exact dependency of the breakup rate on q may be different from $q^{-0.5}$.

Since no accurate measure of the jet shape is known, we make the simplifying assumption, as others have done, that the jet remains circular in cross section, so that $w/A = A^{-0.5}$. Finally, we assume that $C_D = C_D(\gamma, M_\infty) \neq C_D(\alpha)$, and C_D is given by the modified Newtonian theory with $\gamma = 1.4$. With these assumptions, Eq. (13) can be integrated to obtain the following expressions for jet centerline trajectory for normal injection:

For $90° \geq \alpha \geq \alpha_0$, $x = K_5 (\csc \alpha - 1)$

$$y_c = K_5 \ln \cot(\alpha/2) . \qquad (24)$$

For $\alpha < \alpha_0$, $x = K_5(\csc \alpha_0 - 1) + K_6 \ln\frac{\cot(\alpha/2)}{\cot(\alpha_0/2)} - K_7 E(\alpha, \alpha_0)$

$$\qquad (25)$$

$$y_c = K_5 \ln \cot(\alpha_0/2) + E(\alpha, \alpha_0) ,$$

where

$$s_0 = (\epsilon_0 q)^{0.5}; \quad \alpha_0 = \cot^{-1}(s_0/K_5)$$

$$E(\alpha,\alpha_0) = \left(K_6/K_8\right)\ln\left[(K_7 + K_8 - \tan\frac{\alpha}{2})(K_7 - K_8 - \tan\frac{\alpha_0}{2})\right/$$

$$(K_7 - K_8 - \tan\frac{\alpha}{2})(K_7 + K_8 - \tan\frac{\alpha_0}{2})];$$

$$K_5 = \pi q/2C_D; \quad K_6 = (2/\beta)\, q^{0.5};$$

$$K_7 = (K_6 - s_0)/K_5; \quad K_8 = (K_7^2 + 1)^{0.5}.$$

(Note that Eqs. (24) may be combined to give Eq. (21), with $x_0 = y_0 = 0$.)

A major purpose of this analysis is to provide a means for determining the downstream mass distribution of the injectant. If mass torn from the jet is assumed to have negligible y-component of momentum, so that fluid particles remain at a nearly constant y for subsequent values of x, the y distribution of mass can be computed from the theory. The fraction of mass $G(\alpha)$ loss at α (i.e., between α and $\alpha + d\alpha$) is given by:

$$\text{For} \quad 90° \geq \alpha \geq \alpha_0, \quad G(\alpha) = 0\,.$$

(26)

$$\text{For} \quad \alpha < \alpha_0, \quad G(\alpha) = (2/K_6)[(K_5/K_6)\cot\alpha - (s_0/K_6) + 1]^{-2}\,.$$

In addition, the cumulative mass distribution G_α, where G_α is the total mass loss between $\alpha = 90°$ and α, is given by:

$$\text{For} \quad 90° \geq \alpha \geq \alpha_0, \quad G_\alpha = 0\,,$$

(27)

$$\text{For} \quad \alpha < \alpha_0, \quad G_\alpha = 1 - (K_6/2)\, G(\alpha)\,.$$

Both Eqs. (26) and (27) can be combined with Eq. (25) to obtain the corresponding distributions in terms of y, but this is difficult to do explicitly. For completeness, we also include the expression for $s = s(\alpha)$:

For $90° \geq \alpha \geq \alpha_0$, $s = K_5 \cot \alpha$,

(28)

For $\alpha < \alpha_0$, $s = s_0 + K_6 \ln [1 + (K_5/K_6)(\cot \alpha - \cot \alpha_0)]$.

Now, since Clark's data apply to liquid injection into subsonic flow, it might be reasoned that q in the foregoing equations should be more properly interpreted as being the local value of $q' \equiv \bar{q}_j/\bar{q}_s = q/q_s$, where $\bar{q}_s$ is the gas stream dynamic pressure behind the jet interaction shock wave, so that the dynamic pressure loss across the shock would be accounted for. This approach causes some difficulties, however, since $\bar{q}_s$ depends upon the local wave angle, which decreases from $\sim 90°$ (normal shock) in the vicinity of the injector exit down to the Mach angle corresponding to M_∞. Furthermore, the deflection of the freestream flow by the wave to an extent that also varies with the local wave angle means that $\bar{q}_s$ would have to be further modified if only the component of $\bar{q}_s$ in the original freestream direction were of interest. For simplicity, however, it might be assumed that $\bar{q}_s$ and hence, q_s, correspond to the normal-shock condition for M_∞. Then (Ref. 17),

$$q_s = [(\gamma - 1)/(\gamma + 1)] + 2/(\gamma + 1)M_\infty^2 , \qquad (29)$$

and, with the exception of the expression for K_5, q in the foregoing trajectory equations is replaced by (q/q_s) (the q that occurs in the expression for K_5 relates to the drag coefficient, which already accounts for the fact that the flow is supersonic). The effect of this assumption on the theoretical results is examined later.

Before proceeding to test our theoretical model, it is of interest to examine the effect of using an α-

dependent drag prediction. This can easily be done for the case of a constant-area, nondisintegrating jet using the following expressions for the drag on a right circular cylinder:

For $0 \leq M_\infty \leq 1.0$, $C_D = 0.667 (1 + 0.250 M_\infty^2)$,

For $1.0 < M_\infty \leq 1.46$, $C_D = 0.506 + 0.328 M_\infty$,   (30)

For $M_\infty > 1.46$, $C_D = 1.226 - 0.514/M_\infty^2$.

It is shown in Fig. 23 that the above equation closely agrees with the exact, modified Newtonian drag function. For an inclined, cylindrical jet element, M_∞ in Eq. (30) should be replaced by $M_\infty \sin \alpha$, provided it is assumed that the interaction shock shape is identical to the jet boundary shape. The ., when Eq. (30) is substituted into Eq. (13), with $w/A = 1$, expressions for the jet centerline trajectory can be determined. These expressions are not given here because they are lengthy and change their form depending upon M_∞, and they can easily be generated with the use of available integral tables. However, Fig. 26 compares some trajectory calculations based on them with those based on a drag model in which $C_D = C_D (M_\infty)$ (i.e., no α dependency) is assumed. It is seen that the effect of the α-dependent model is to increase the predicted jet penetration at the low Mach number ($M_\infty = 1.6$) at low q (q = 3). For q = 30, the effect is smaller, and for q = 100, it is negligible. For the higher Mach number ($M_\infty = 5$), the effect is negligible even at low q.

D. COMPARISON OF PRESENT ANALYSIS TO DATA

In Fig. 27a the present analysis is compared to the empirical Eq. (1) for jet boundary penetration (dashed curve) using $\epsilon_0 = 2$ and $\beta = 2.1$ (these values were previously shown to give a good fit to Clark's data). In general, the predicted curves fall far below the curve given
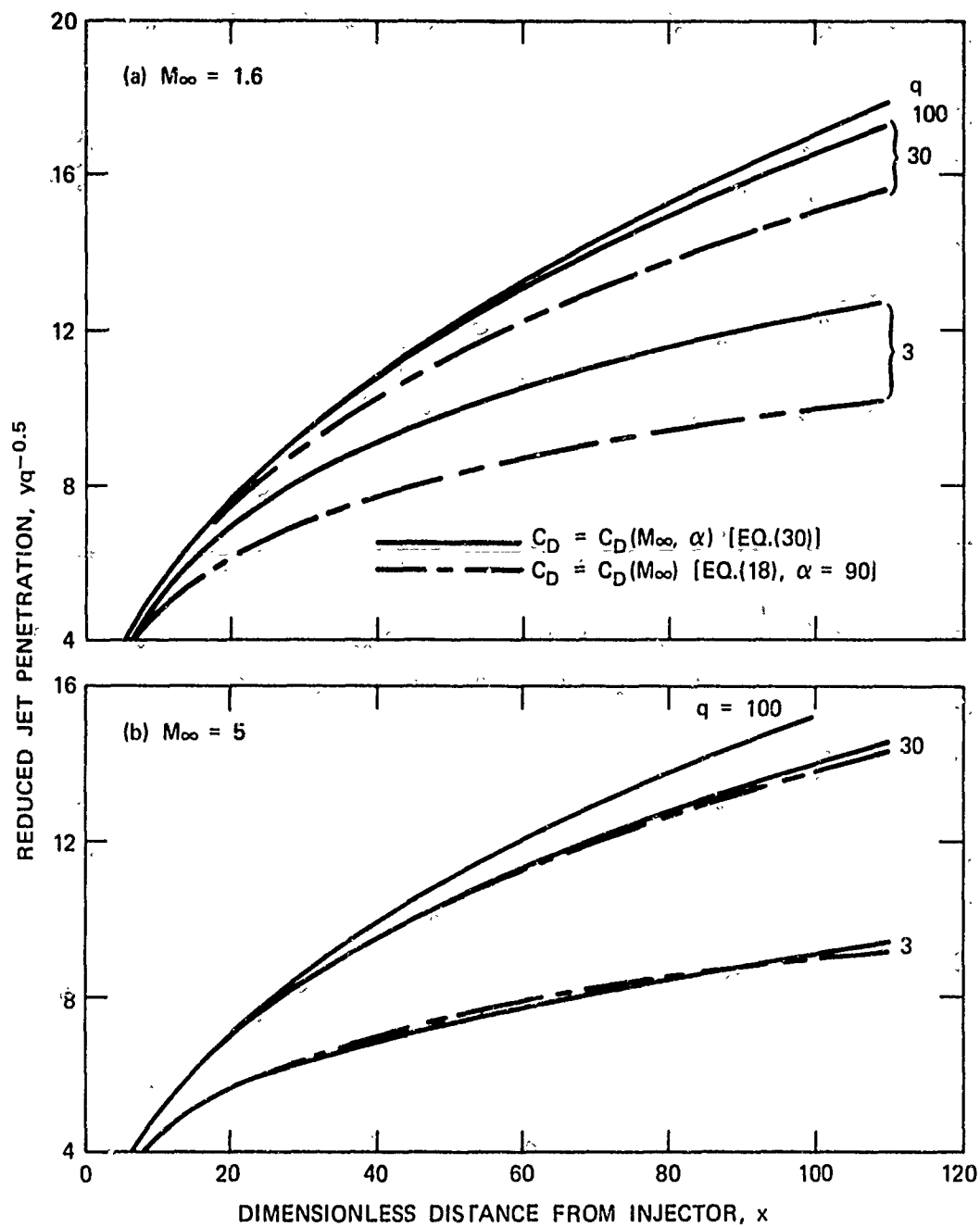
FIGURE 26   EFFECT OF DRAG MODEL ON PREDICTED JET PENETRATION

- 62 -

by Eq. (1), suggesting that the disintegration rates used are excessively high, with a dependency on q that was not seen from the photographic data, and it is noted that this q-dependency is the reverse from that predicted in Ref. 8. Finally, Fig. 27a shows a slight reduction in penetration when M_∞ is increased from 1.6 (solid curves) to 5 (dash-dot curves). This result is interesting, since the photographic results shown in the last part of Fig. 6 indicate a sizable effect in this direction (reduced penetration) for a smaller change in M_∞ (increase from 1.62 to 2.72). In view of the limited accuracy of the photographic data, however, it is felt that more extensive tests are required to establish firmly the M_∞ effect.

If ϵ_0 is kept at 2, but β is decreased to 0.65 (the variation of A with s predicted with this value is compared to Clark's data in Fig. 24), an improved overall fit between theory and data is obtained as seen in Fig. 27b. Although the discrepancy at low q is reduced, a larger effect of q is predicted, as well as a slightly increased dependency on M_∞. Figure 27c presents the theoretical predictions for the case where the disintegration rate is based on conditions existing behind the interaction shock, again using $\epsilon_0 = 2$ and $\beta = 2.1$. The overall spread of the various curves about the curve from Eq. (1) is no better than in part (b), and the effect of M_∞ at a given q is now reversed (opposite to the trend seen in Fig. 6).

From these results we conclude that ϵ_0 and β must somehow depend on q. At this point, one could perform a numerical experiment to ascertain these dependences on q. However, since we are more concerned with predicting the cumulative injectant mass distribution G_y, we chose to make use of the available experimental G_y's.

For this purpose, it is expedient to set ϵ_0, whose effect on the predicted penetration is secondary to that of β, at a fixed value for given conditions of injection, and then seek the value of β that gives the best agreement
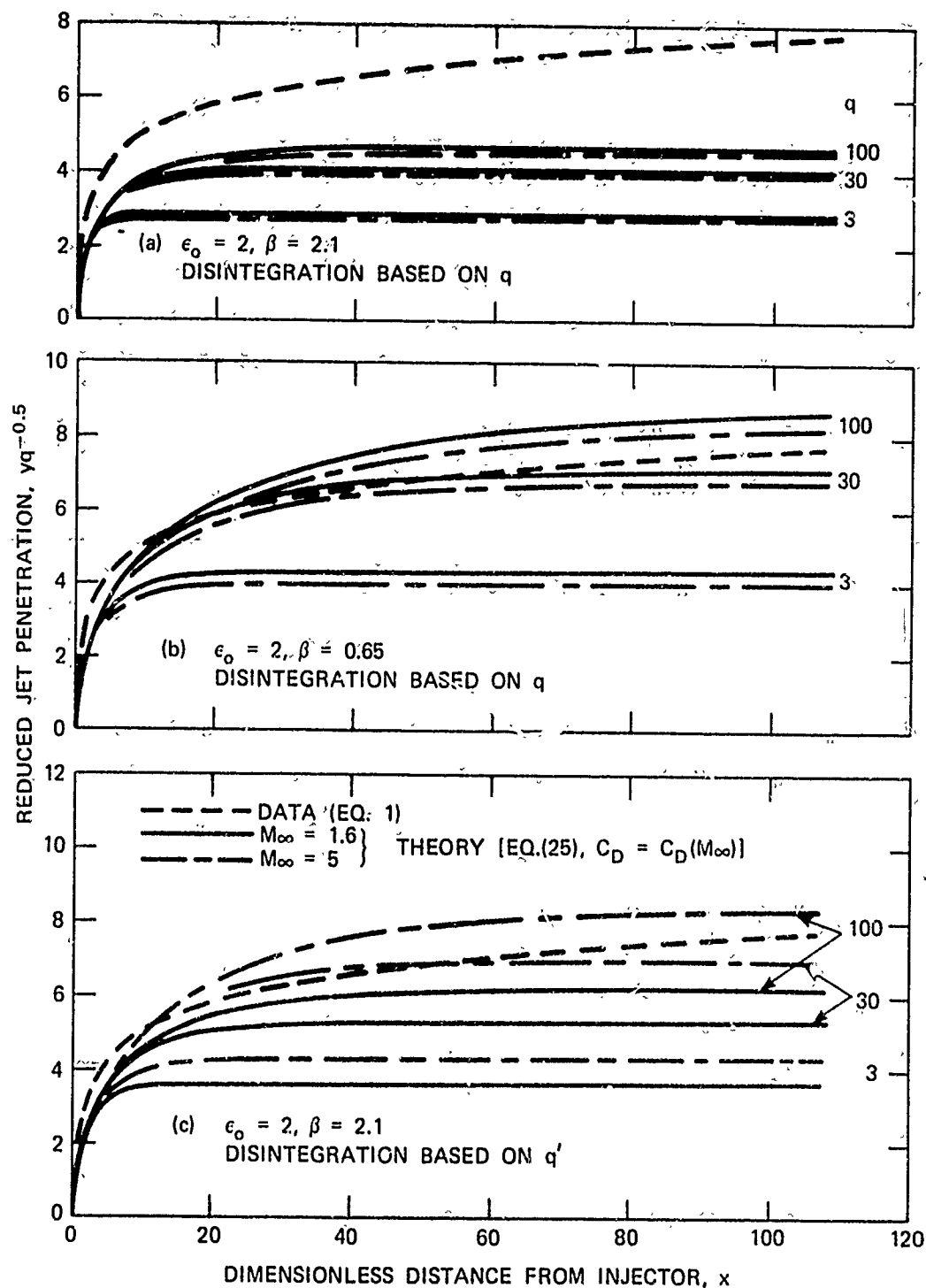
FIGURE 27   COMPARISON OF EMPIRICAL AND THEORETICAL JET
TRAJECTORIES

between theory and data. This value of ϵ_0 was chosen to reproduce the point on the y-axis intercepted by a line that (a) has the same slope as that at the inflection point (i. e., $d^2G_y/dy^2 = 0$) of the experimental G_y curve and (b) passes through the inflection point. The values of y determined visually in this manner are 1.3 for q = 3.1 (Test 13) and 4.2 for q = 10.3 (Test 12) (see Fig. 28). The corresponding values of ϵ_0 are 0.55 and 1.75, respectively, when the disintegration model is based on q, and 0.15 and 0.50 when the model is based on q'.

Using the above values of ϵ_0, various values of β were tried. Figure 28 shows the theoretical G_y-distributions for narrow ranges of β to show their sensitivity to β. With an appropriate β, agreement is good in the region between 20 and 80%. For the q = 10.3 data in Fig. 28, ϵ_0 = 1.75 and $\beta \simeq 0.30$ give a good fit when the breakup model is based on q. The values of ϵ_0 and β based on Clark's data (2 and 2.1) give a poor fit, which is only slightly improved when β is decreased to 0.65. For the q = 3.1 data, ϵ_0 = 0.55 and $\beta \simeq 0.20$ give the best fit for the q-based breakup model. The values of ϵ_0 and β determined for the q = 10.3 data do not give as good a fit here, which further suggests that ϵ_0 and β are functions of q. As shown in parts (c) and (d) of Fig. 28, the breakup model based on q' gives about equally good agreement when the previous values of ϵ_0 are reduced by the ratio, q/q', and different values of β are used. Again the agreement is poor for ϵ_0 = 2 and β = 2.1, and it is degraded when an attempt is made to fit both the q = 3.1 and 10.3 data with the same values of ϵ_0 and β.

The sets of ϵ_0, β that have been shown to give good data fits (1.75, 0.30 for q = 10.3; 0.55, 0.20 for q = 3.1; 0.49, 0.55 for q' = 36.9; and 0.15, 0.35 for q' = 11.1) can now be used in an attempt to formulate a dependency of ϵ_0 and β on q or q'. Taken at face value, the above results suggest that $\epsilon_0 \propto q^{0.96}$, $\beta \propto q^{0.35}$, $\epsilon_0 \propto (q')^{0.96}$, and $\beta \propto (q')^{0.45}$. The q = 10.3 data were
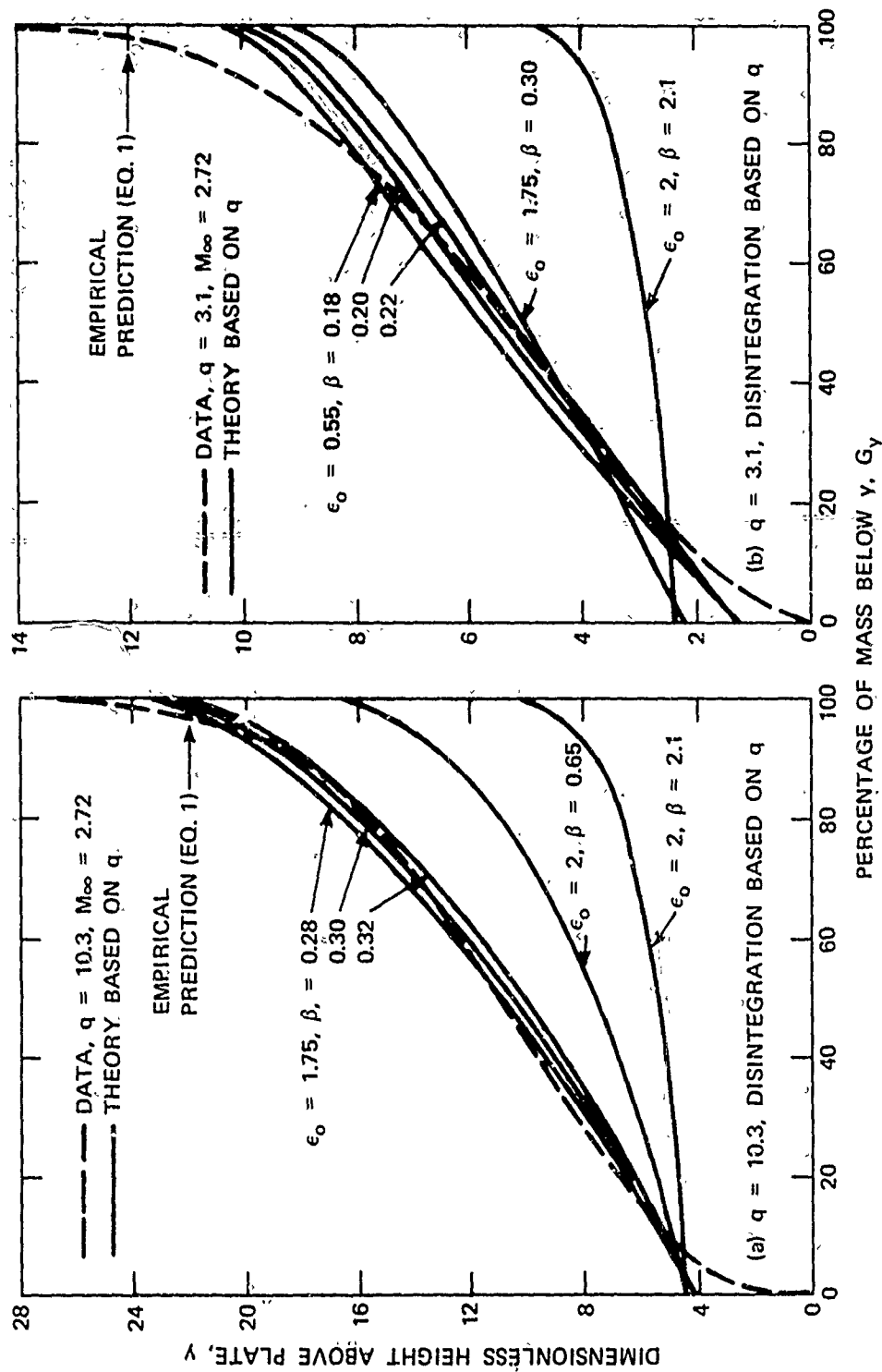
- 65 -

FIGURE 28   COMPARISON OF EXPERIMENTAL AND THEORETICAL
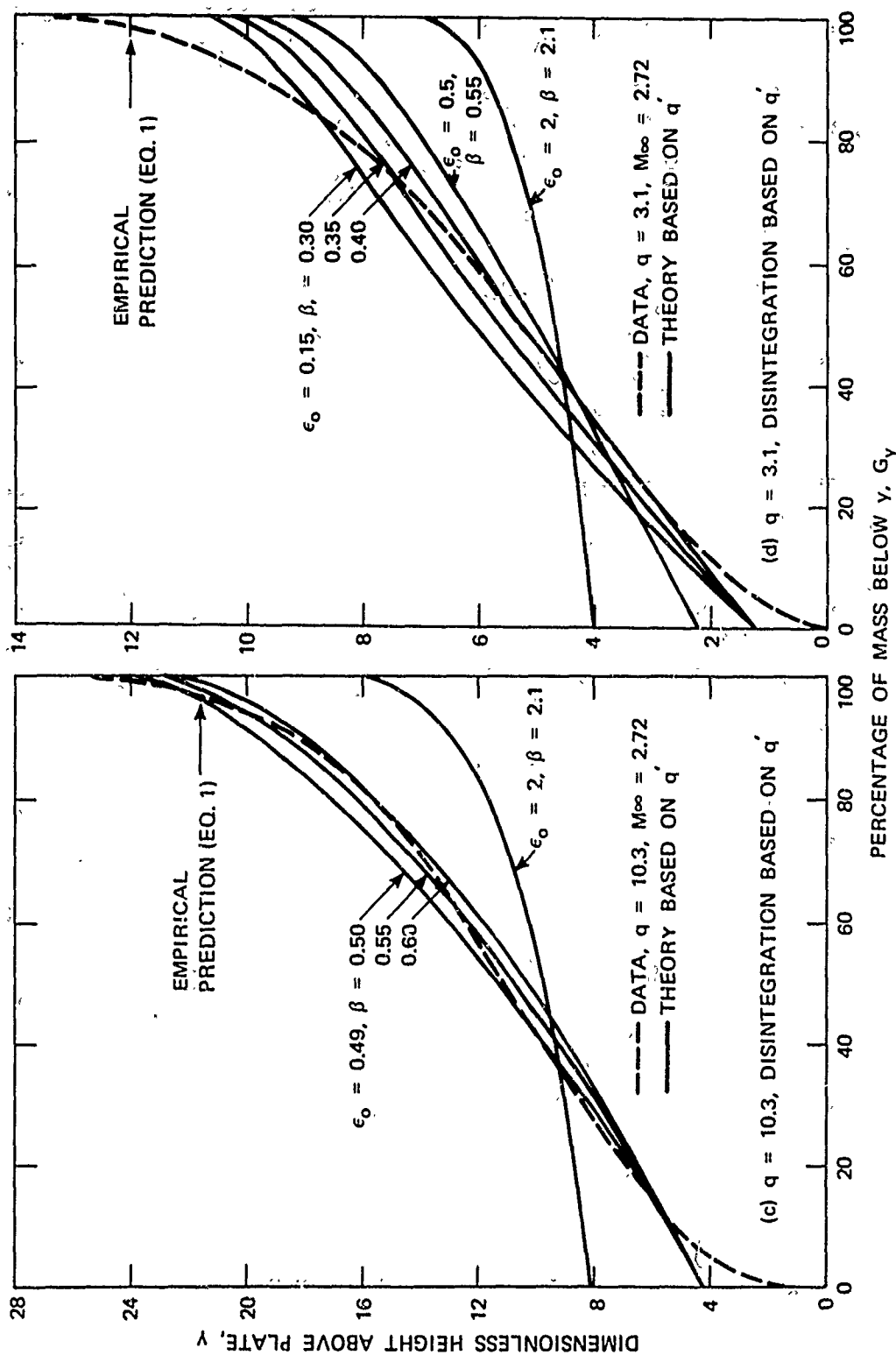ACCUMULATIVE DISTRIBUTIONS FOR INJECTANT MASS

FIGURE 28 (CONCLUDED)

used to determine the proportionality constants in the foregoing expression. When this was done, it was found, by comparing the predicted and empirical jet trajectories, that the predicted values for ϵ_0 were excessively high for large q or q'. In addition, the values of β appeared to be too low for large q or q', particularly for the q-based β. In view of these results, and based on the experience gained in judging the effects of ϵ_0 and β on the predicted trajectories, the following functional forms of ϵ_0 and β were assumed: $\epsilon_0 \propto \beta \propto q^{0.5}$ and $\epsilon_0 \propto \beta \propto (q')^{0.5}$. To maintain agreement with the experimental results for G_y, the q = 10.3 data were used to compute the proportionality constants which resulted in the following equations:

$$\epsilon_0 = 0.545 \, q^{0.5}; \, \beta = 0.094 \, q^{0.5},$$

and   (31)

$$\epsilon_0 = 0.082 \, (q')^{0.5}; \, \beta = 0.091 \, (q')^{0.5}.$$

The trajectories predicted with the use of Eqs. (31) are shown in Fig. 29 for q values between 3 and 100 and M_∞ = 1.6 and 5.0. The overall improvement compared to Fig. 27 is obvious for both breakup models. The spread of the theoretical trajectories about the empirical curve (generally high for q ≥ 30, low for q = 3) is of the same order of magnitude as the scatter of the photographic data on which the empirical equation is based (see Fig. 7). Hence, there is no firm basis for much further evaluation of the theoretical results in terms of their predicted dependency on q and M_∞. Moreover, there is little to choose between the breakup models. For the q-based model, the predicted penetration is nearly independent of M_∞ for q ≥ 30, whereas for the q'-based model, it increases with M_∞ for q ≥ 30. We do not have a sufficient basis for judging whether this may be a point against the q'-based model.

We have already seen in Figs. 28a and c the extent to which the values of ϵ_0 and β given by Eqs. (31) give a fit to the q = 10.3 data. The extent to which the
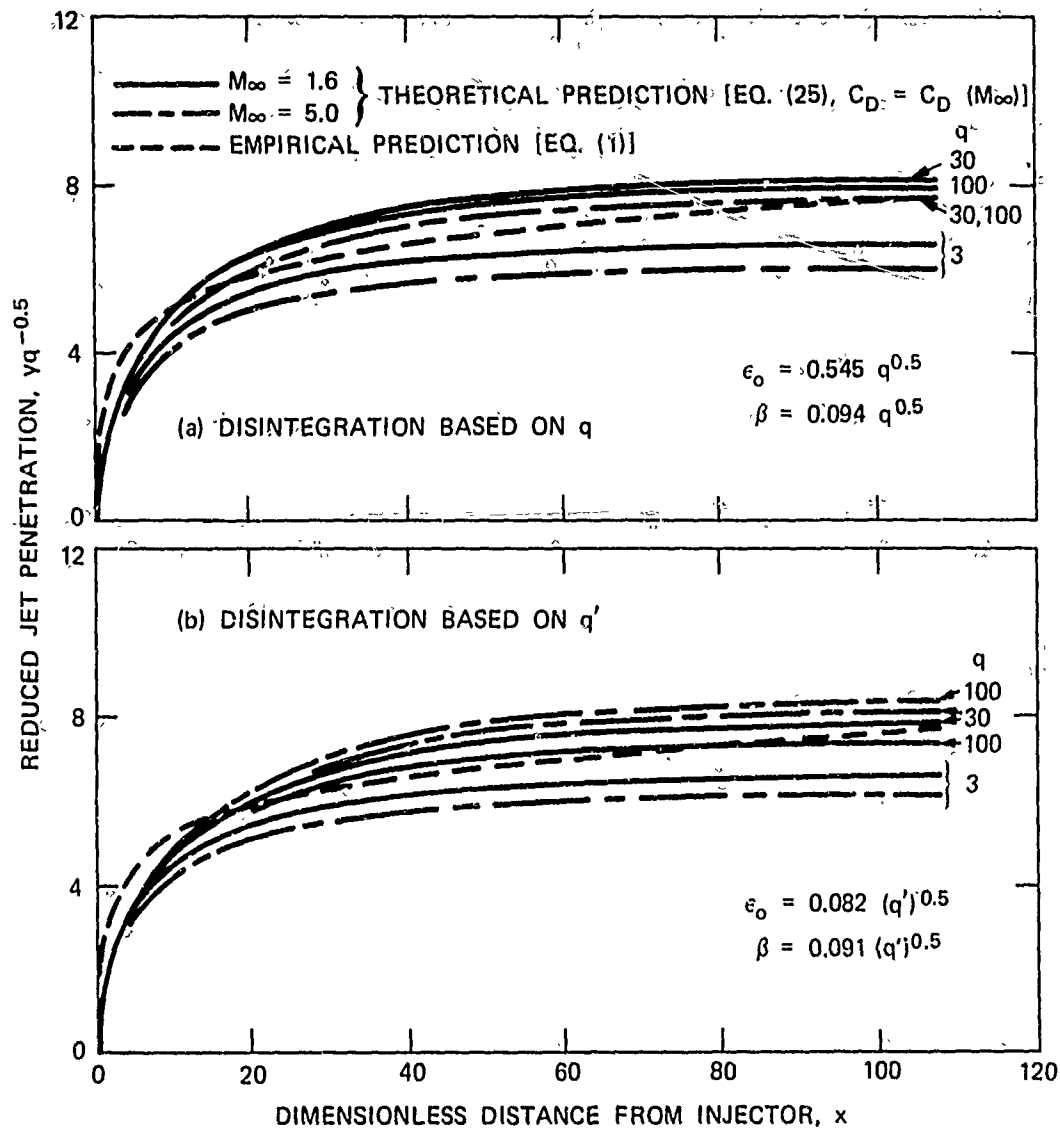
FIGURE 29   COMPARISON OF EMPIRICAL AND THEORETICAL JET TRAJECTORIES
            USING IMPROVED JET BREAKUP MODEL

- 69 -

q = 3.1 data are also fitted is shown in Fig. 30. The predicted $\bar{G}_y$ at a given y tends to be lower then the experimental value except near the jet boundary. However, the fit is considered reasonably good, especially when the experimental difficulty in sampling is remembered.

Up to this point, we have considered only the experimental distributions for G_y, without considering the distributions for $G(y)$, the percentage of mass at a level y, because the G_y distributions are less sensitive to the exact details of the jet breakup model and, hence, are more useful for comparing with experiment. However, Fig. 31 compares the theoretical distribution for $G(y)$, computed using the q-based breakup model (the result obtained with the q'-based model is nearly identical), with the experimental result for the q = 3.1 case. The effect of assuming that jet breakup is delayed for a finite distance is clearly shown by the disagreement at small y, where the greatest difference between theory and experiment exists.

An important question that must be answered now is whether the jet area variations predicted by Eqs. (31) agree with Clark's data. Figure 32 shows that for q' $\geq$ 100 (or q $\geq$ 30), the q'-based breakup model predicts values for A that are consistent with the data, and it falls down only at low q, whereas the q-based model gives poorer agreement at all q levels. Therefore, the q'-based model, which approximately accounts for the dynamic pressure losses across the interaction shock, is judged to be the more appropriate one to use, especially if subsonic data such as Clark's are to be related to supersonic data. The ability to derive a breakup model based on the present data that is also consistent with previous data is particularly satisfying, since this gives confidence in, at least, the qualitative value of the present data.

We have now established that, excepting low values of q (q $\approx$ 3), good agreement exists between theory
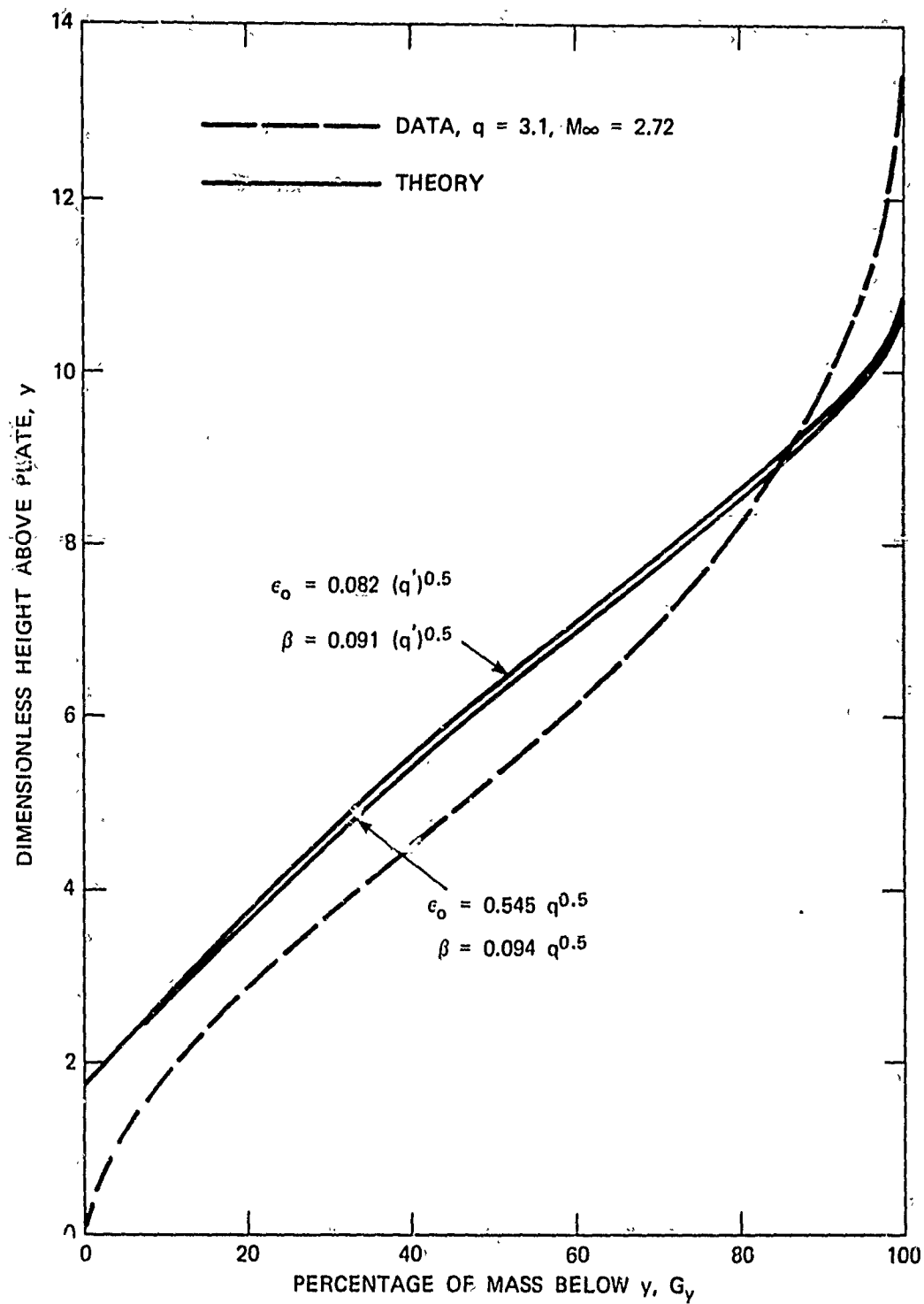
FIGURE 30   COMPARISON OF EXPERIMENTAL AND THEORETICAL
ACCUMULATIVE DISTRIBUTION FOR INJECTANT MASS
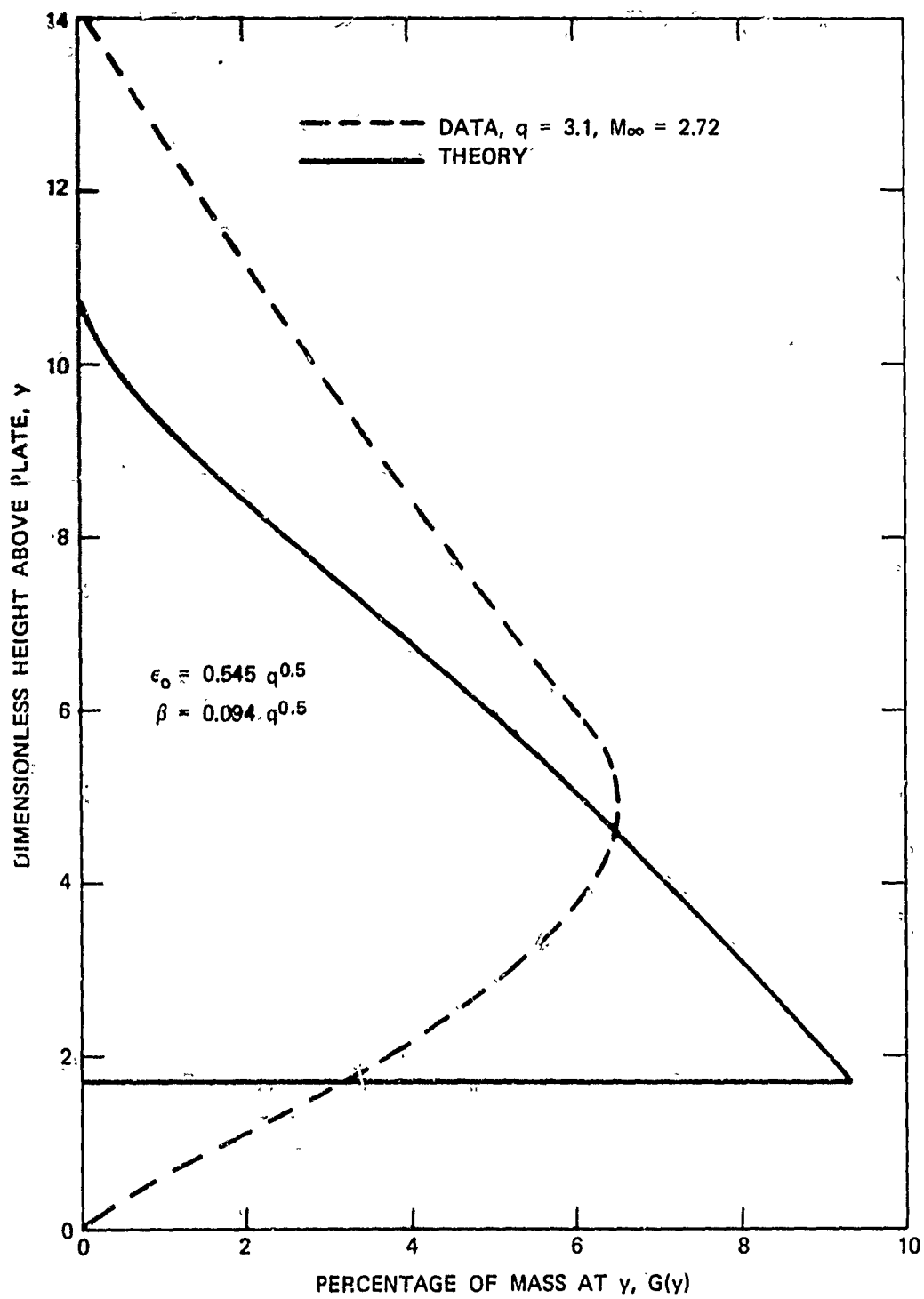USING IMPROVED JET BREAKUP MODEL

- 71 -

FIGURE 31   COMPARISON OF EXPERIMENTAL AND THEORETICAL
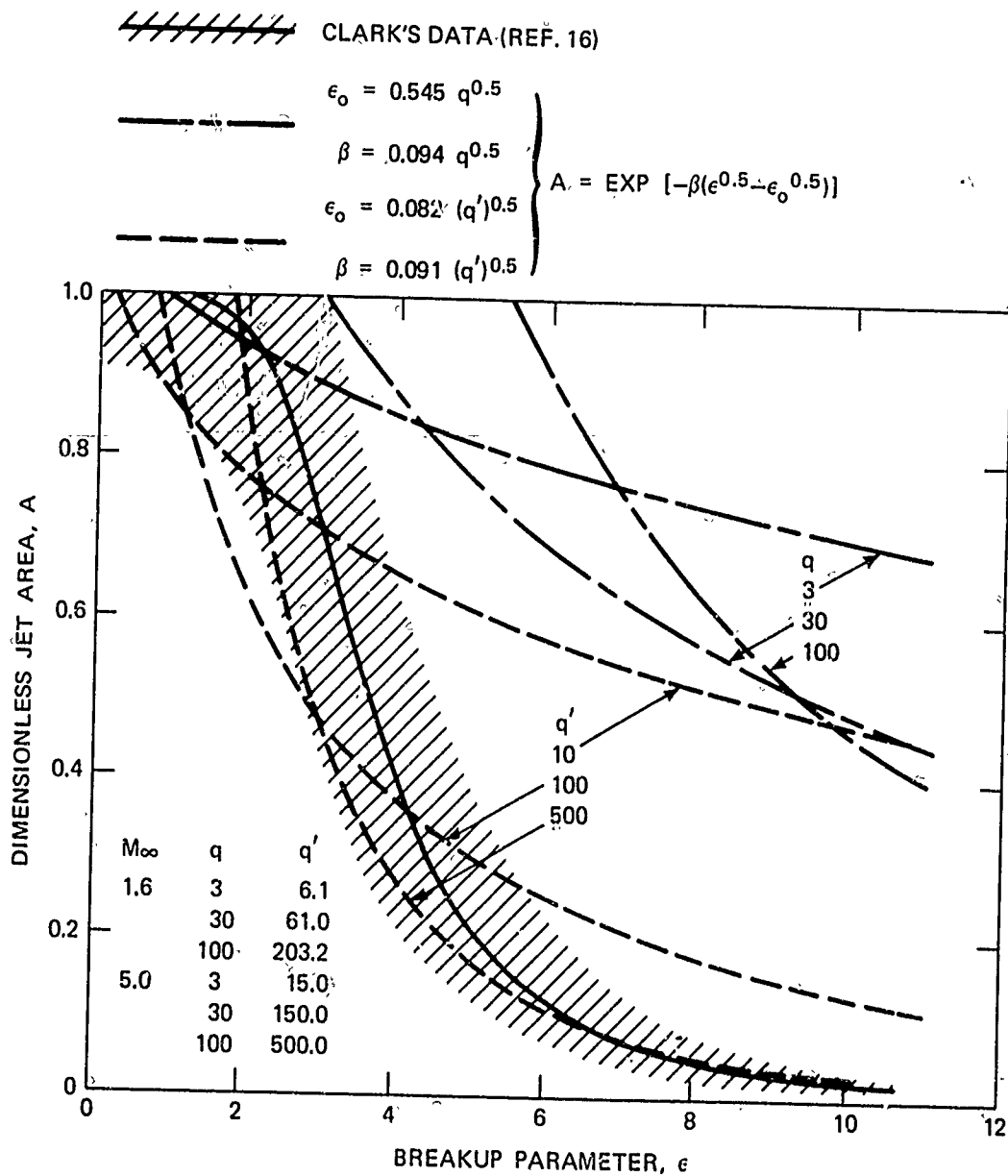DISTRIBUTIONS FOR INJECTANT MASS

FIGURE 32   COMPARISON OF IMPROVED JET BREAKUP MODEL
WITH CLARK'S DATA

and data, in terms of either predicted jet boundary location or injectant mass y-distribution. It is desirable to consider possible explanations for the discrepancies at low q, which, primarily, have appeared as low predicted boundary locations. One feature of the injection process that has not been considered heretofore is the mass diffusion and turbulent mixing effect which obviously contributes to the dispersion of the injectant, particularly in the jet boundary region. Perhaps this effect is relatively more important for a low-q jet, which has lower absolute values of penetration than a higher-q jet.

A final observation concerning the jet breakup model deals with the rate expression given in Eq. (23):

$$dA/ds = -\beta q^{-0.5} A . \tag{23}$$

With $\beta \propto q^{0.5}$, as assumed herein, the above expression reduces to $dA/ds \propto A$, i. e., following the path of a jet element, the disintegration rate depends only on the local cross-sectional area. Intuitively, it seems that dynamic conditions of the jet and the airstream should affect the disintegration rate. The failure of the finalized form of the theory to predict such effects is taken as another indication that the q-dependency assumed for various parameters might be incorrect. There is certainly a need to obtain considerably more detailed flowfield data for a variety of conditions to establish a basis for improving the theory.

SECTION VI

SUMMARY AND CONCLUSIONS

The dispersion of a liquid jet that was injected transversely from a flat-plate surface into a supersonic airstream was studied by photographic and in-stream-probe measurements. The data were used to derive empirical correlations for predicting jet boundary penetration and spreading and as the basis for the development of a theoretical model that gives a satisfactory prediction of the transverse distribution of jet mass.

The photographic measurements, which were based on back-scattered light, were obtained for the injection of water and isopropyl alcohol from orifices with diameters of 0.017, 0.027, and 0.052-inch into airstreams having Mach numbers of 1.62 and 2.72. Jet/freestream dynamic pressure ratio (q), jet Reynolds and Weber numbers, and freestream Reynolds number were varied by factors of 8, 10, 11, and 3, respectively, in the jet penetration tests, and by factors of 23, 4, 9, and 5 in the jet spreading tests. The penetration results are correlated to within $\pm$ 10% by an empirical equation which predicts that dimensionless penetration (referenced to the effective orifice diameter) at a dimensionless downstream distance varies only with $q^{0.5}$. No other clearcut dependency of penetration on either the Reynolds or Weber numbers or the physical properties of the fluids was observed. The dimensionless maximum jet width was correlated to within $\pm$ 7.5% by an empirical equation which predicts a dependency only on $q^{0.25}$ (equally-good agreement was obtained by replacing q with the jet plenum-to-freestream static pressure ratio). The empirical correlation for jet penetration developed from these data is in reasonably good quantitative agreement only with existing empirical correlations that also are based on q; the agreement is within the $\pm$ 20% variation that was found to be

possible as a result of differences in photographic techniques that could occur from program to program. However, a logarithmic dependency of jet height on downstream distance, predicted from the present correlation, shows improved qualitative agreement with the data as compared to the previous correlations, which generally predict a power-law dependency. The jet widths determined from the present correlation are only $\frac{1}{3}$ to $\frac{1}{2}$ as large as those given by prior correlations, but they are substantiated by our mass-sampling data.

For the purpose of sampling a heterogeneous stream, a resistance-heated probe and a heated gas chromatograph system were developed. Although evaluation tests of the probe showed that it gave an incorrectly high value of injectant concentration under conditions of high liquid loading in the test stream, the system was deemed to yield useful qualitative results. Mass-sampling, pitot-pressure and cone-static-pressure surveys were made at a downstream distance of 50 jet diameters in two tests with an airstream Mach number of 2.72 and with trichlorofluoromethane as the injectant, and flowfield properties were deduced on the assumption that the injectant occurred as all vapor at the sampling location. The total injectant flow rates deduced from the data exceed the input values by 58% in one test and 28% in the other; these values are twice as high when the injectant is assumed to occur in the liquid phase. Accepting the qualitative value of the all-vapor results, they show that 65 to 70% of the mass is below the jet half-height, and 75 to 85% of it is within the central jet half-width. In addition, the cumulative mass distributions for either the transverse or lateral directions from the two tests are nearly similar when the respective distances are referenced to either jet height or jet width, even though the absolute downstream distances differed by a factor of 2 (different orifice sizes and injection pressures were used in the two tests). This fact suggests that the present data are useful for estimating injectant mass distributions for conditions quite different from those used in

the tests. The sampling data, which give rather accurate measures of jet height and width, showed that the photographically-based empirical correlations summarized above give slightly low values, but that they account for at least 96% of the injectant mass, and that the injectant that occurs outside the empirically predicted boundaries is at a concentration that is probably too low to be detected by ordinary photographic procedures.

Existing theoretical treatments that include the effect of jet disintegration give reasonable predictions for jet penetration, but they neither allow an assessment of the effects of various necessary assumptions nor provide for deducing mass distribution. An analysis was developed on the assumptions that: (a) the jet is a circular, disintegrating body, (b) its drag can be based on the modified Newtonian theory, (c) its local cross-sectional area can be based on Clark's (Ref. 16) data for jet disintegration in a subsonic stream, and (d) particles torn from the jet remain at a constant transverse position for subsequent downstream locations. The predicted transverse distributions of mass agree reasonably well with the data when the jet disintegration parameters appearing in the analysis are based on approximate conditions existing behind the j ', interaction shock. The predicted jet boundary trajectories show dependencies on q and free-stream Mach number that were not established from the photographic data, but these effects are comparable in magnitude to the scatter of the photographic data.

The detailed flowfield data have proven to be extremely valuable for describing liquid jet disintegration. Additional effort is required to improve the accuracy of the mass-sampling probe, and additional mass-sampling data for a wide variety of test conditions are needed for further assessment and improvement of the theory.

SECTION VII

REFERENCES

1. L. J. Chelko, Penetration of Liquid Jets into a High Velocity Air Stream, NACA RM E50F21, August 1950.

2. E. L. Geery and M. J. Margetts, "Penetration of a High-Velocity Gas Stream by a Water Jet," Journal Spacecraft and Rockets, Vol. 6, No. 1, January 1969, pp. 78-81.

3. F. P. Provinelli, Displacement of Disintegrating Liquid Jets in Crossflow, NASA TN D-4334, February 1968.

4. M. W. Dowdy and J. F. Newton, Jr., Investigation of Liquid and Gaseous Secondary Injection Phenomena on a Flat Plate with M = 2.01 to M = 4.54, Jet Propulsion Lab. TR 32-542, 23 December 1963.

5. R. P. McRae, Experimental Investigation of a Liquid Jet Injected into a Mach 4 Stream, Douglas Aircraft Co. Report SM-47879, May 1966.

6. J. M. Forde, S. Molder, and E. J. Szpiro, "Secondary Liquid Injection into a Supersonic Airstream," AIAA Journal, Vol. 3, No. 8, August 1966, pp. 1172-1176.

7. M. A. Kolpin, K. P. Horn, and R. E. Reichenback, "Study of Penetration of a Liquid Injectant into a Supersonic Flow," AIAA Journal, Vol. 6, No. 5, May 1968, pp. 853-858.

8. I. Catton, D. E. Hill, and R. P. McRae, "Study of Liquid Jet Penetration in a Hypersonic Stream," AIAA Journal, Vol. 6, No. 11, November 1968, pp. 2084-2089.

Preceding page blank

REFERENCES (cont'd)

9. R. W. Castle, Jr., <u>An Investigation of Penetration and Spreading for Various Fluids Injected into a Supersonic Stream</u>, Masters Thesis, Naval Postgraduate School, March 1968.

10. W. F. Hinson, P. B. Gooderum, and D. M. Bushnell, <u>Experimental Investigation of Multiple-Jet Liquid Injection into Hypersonic Flow</u>, NASA TN D-5861, June 1970.

11. K. P. Horn and R. E. Reichenback, "Further Experiments on Spreading of Liquids Injected into a Supersonic Flow," <u>AIAA Journal</u>, Vol. 7, No. 2, February 1969, pp. 358-359.

12. R. D. Ingebo, <u>Penetration of Drops into High-Velocity Airstreams</u>, NASA TM X-1363, April 1967.

13. M. Adelberg, "Breakup Rate and Penetration of a Liquid Jet in a Gas Stream," <u>AIAA Journal</u>, Vol. 6, No. 8, August 1967, pp. 1408-1415.

14. C. L. Yates, "Liquid Injection into Supersonic Airstreams," AIAA Paper 71-724, Salt Lake City, Utah, June 1971.

15. S. F. Hoerner, <u>Fluid-Dynamic Drag</u> (published by the author), 1965.

16. B. J. Clark, <u>Breakup of a Liquid Jet in a Transverse Flow of Gas</u>, NASA TN D-2424, August 1964.

17. A. H. Shapiro, <u>The Dynamics and Thermodynamics of Compressible Fluid Flow</u>, The Ronald Press Co., New York, 1954.

REFERENCES (cont'd)

18. Z. Kopal, Tables of Supersonic Flow Around
     Cones, M. I. T. Tech. Report No. 1, 1947.

19. E. F. Blick, R. R. Walters, and C. Von Rosen-
     berg, "Similarity Rule Estimation Methods for
     Cone Flow with Variable Gamma," AIAA Journal,
     Vol. 6, No. 5, May 1968, pp. 959-961.

APPENDIX

EXPERIMENTAL PRESSURE DATA AND FLOWFIELD DATA REDUCTION TECHNIQUE

Figure A-1 presents the pitot-pressure data for Tests 11-13 at $x/d_j = 50$, and Fig. A-2 presents the corresponding cone-static pressure data.

FLOWFIELD DATA REDUCTION TECHNIQUE

The method used to deduce flowfield properties from the instream probe data is based on the following assumptions:

1. The experimental probes respond only to the axial motion of the flow, or, equivalently, the motion is one-dimensional,

2. The gas phase flow can be measured and computed independently of the presence of the liquid phase,

3. The portion of the injectant that vaporizes is in thermal and dynamic equilibrium with the air, and

4. The mean flow is steady.

The pressure coefficient of the cone-static-pressure probe is given by:

$$C_p = (p_c - p)/(\gamma p M^2 / 2) , \qquad (A-1)$$

where p_c is the average of the four cone surface-pressure measurements. Values of C_p, which are determined from solutions of the Taylor-Maccoll differential equation for subsonic flow around cones, are given in Ref. 18 for various values of the cone half-angle and M, but only for values of $\gamma = 1.4$ and 1.33. Fortunately, however, C_p is
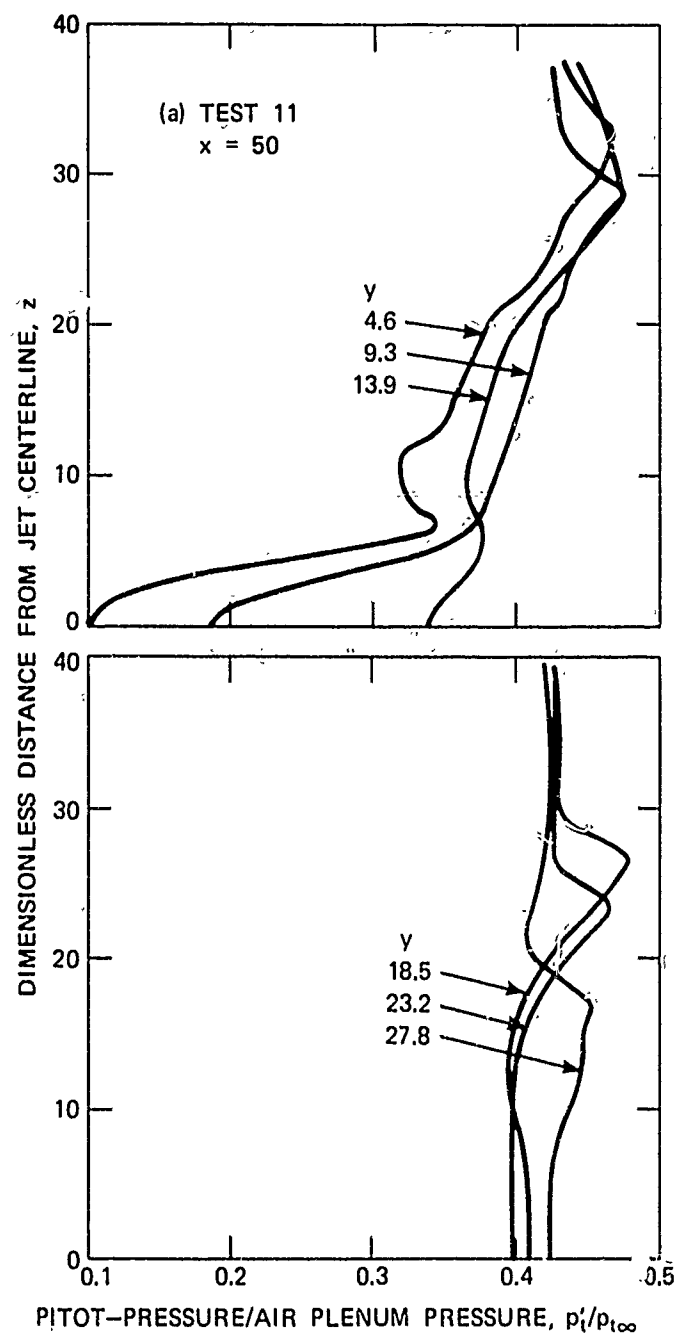
Preceding page blank

FIGURE A-1 PITOT-PRESSURE DATA

The axes of the figure are labeled: vertical axis "DIMENSIONLESS DISTANCE FROM JET CENTERLINE, z"; horizontal axis "PITOT-PRESSURE/AIR PLENUM PRESSURE, $p_t'/p_{t\infty}$".

Top panel: (a) TEST 11, x = 50, with curves labeled y = 4.6, 9.3, 13.9.

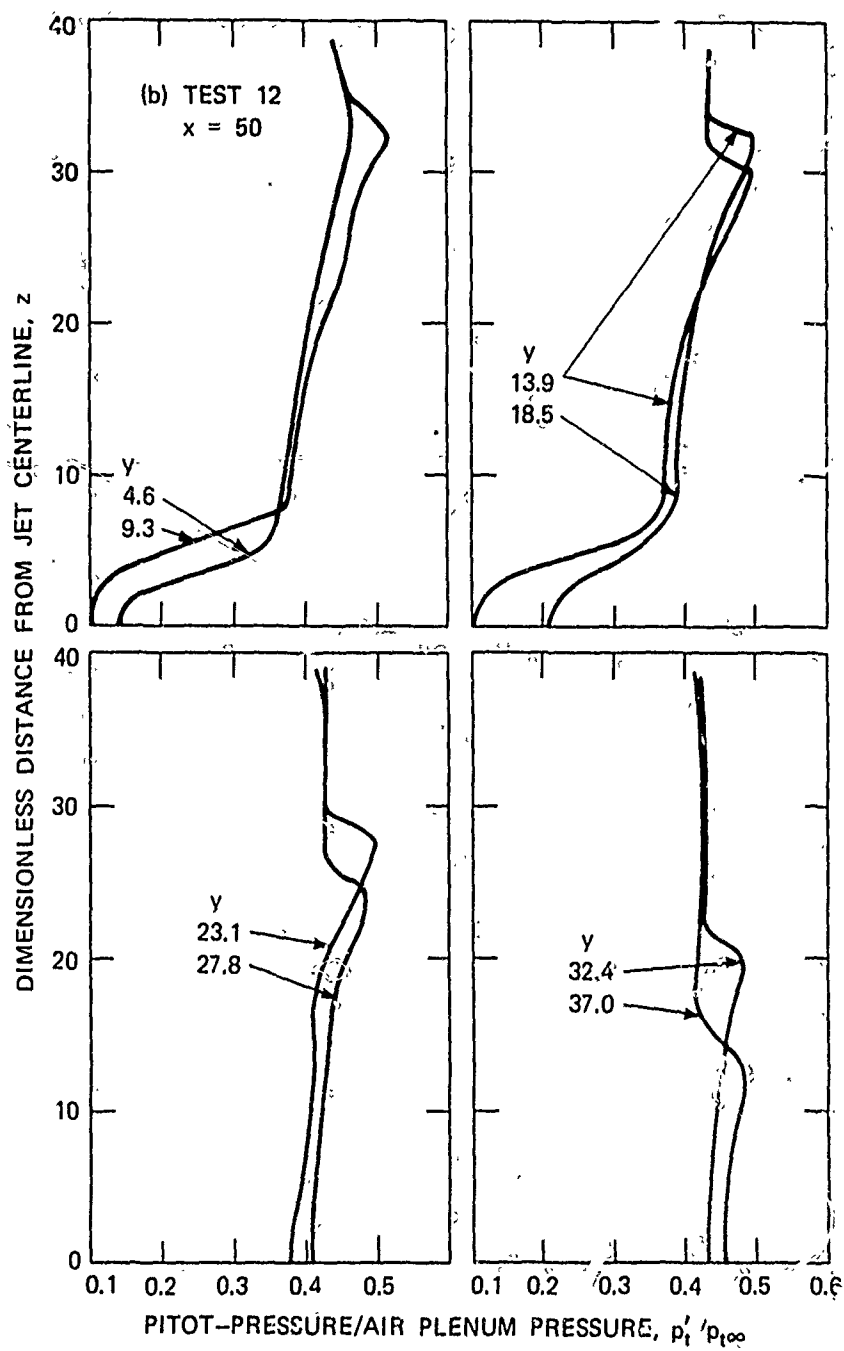Bottom panel: curves labeled y = 18.5, 23.2, 27.8.
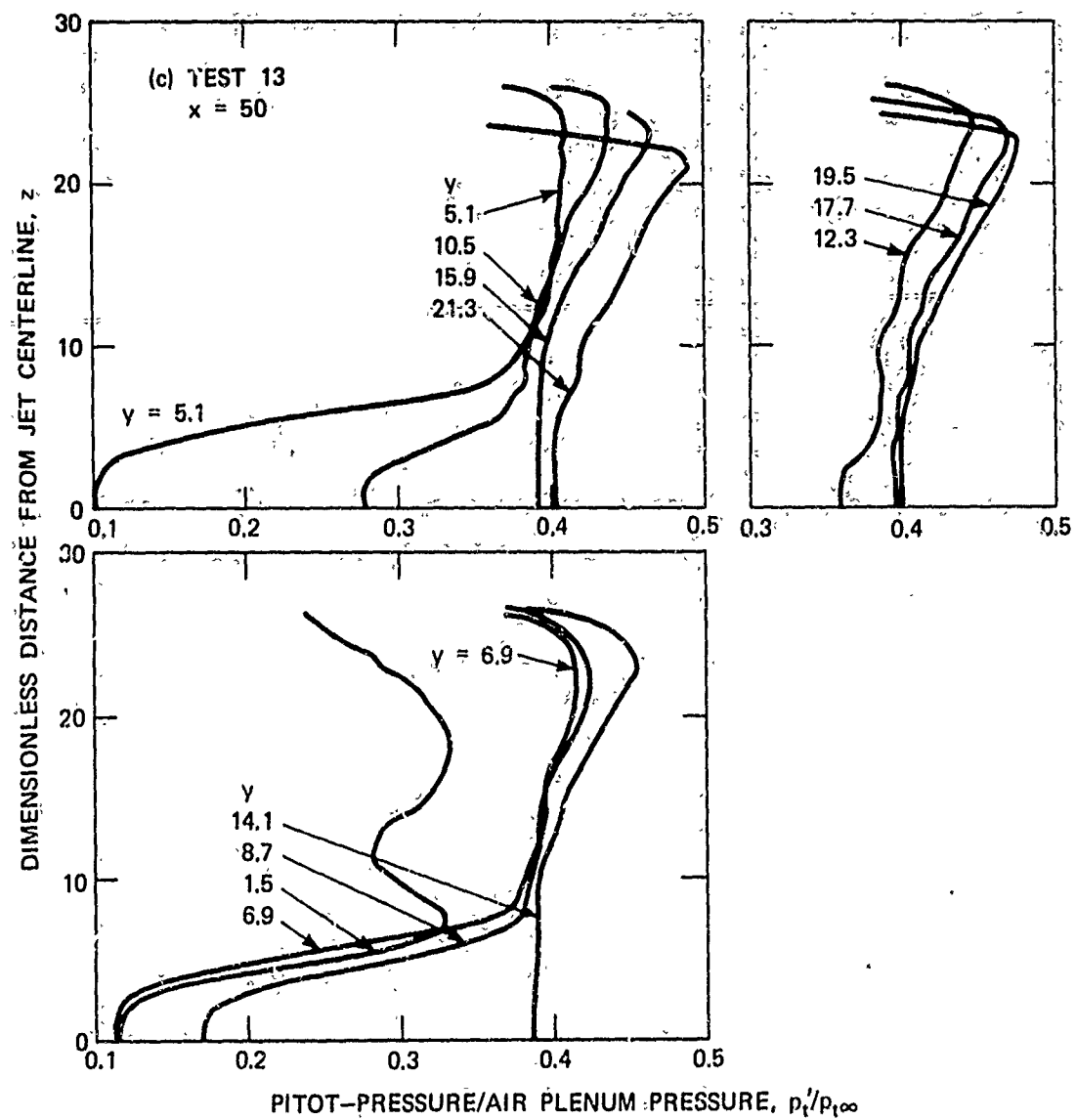
FIGURE A–1   (CONTINUED)
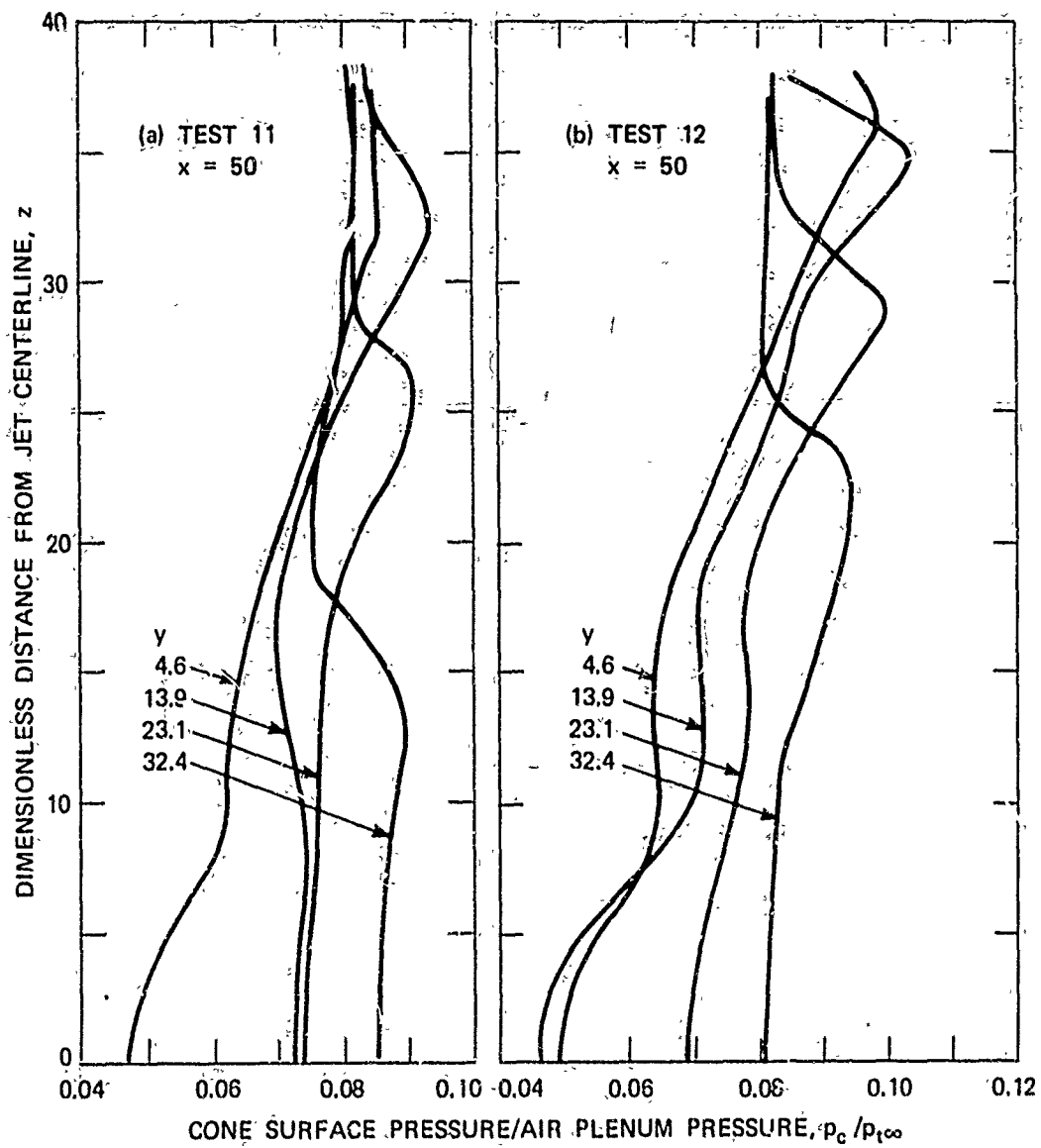
FIGURE A-1   (CONCLUDED)
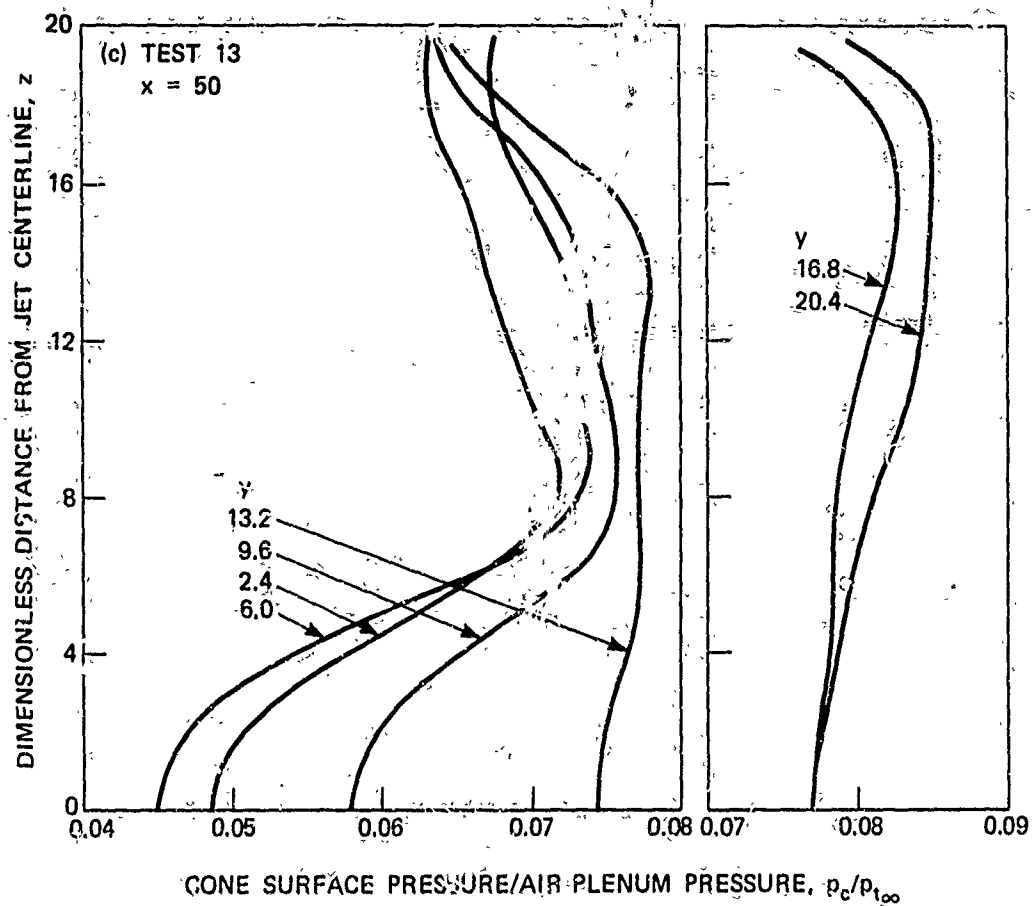
FIGURE A-2   CONE-STATIC-PRESSURE DATA

FIGURE A-2 (CONCLUDED)

quite insensitive to γ (see Ref. 19) and the values applicable to $\gamma = 1.4$ are used herein. The measured pitot-pressure is introduced into Eq. (A-1), and the equation is rewritten as:

$$p_c/p_t' = (p/p_t')[1 + (\gamma M^2 C_p/2)] . \qquad (A-2)$$

A relation for p/p_t' is given by the Rayleigh pitot formula (Ref. 17):

$$p/p_t' = \left\{ \frac{2\gamma M^2/(\gamma + 1) - (\gamma - 1)/(\gamma + 1)}{[(\gamma + 1)M^2/2]^\gamma} \right\}^{1/(\gamma-1)} . \qquad (A-3)$$

With Eqs. (A-2) and (A-3) and the values of C_p as a function of M, a plot of p_c/p_t' as a function of γ and M can be derived, from which M can be determined once γ is specified. Then, p is determined from a plot of Eq. (A-1), written as follows:

$$p/p_c = [1 + (\gamma M^2 C_p/2)]^{-1} . \qquad (A-4)$$

The procedure beyond this point depends upon whether the phase of the injectant is assumed to be all liquid or all vapor. (Actually, one could consider the more general case where only a portion of the injectant was vaporized; then, however, it is necessary to specify the velocity of the condensed phase, which is generally unknown.) We shall consider these two cases separately.

ALL VAPOR

When the injectant occurs as all vapor, the mass-sampling measurement, which gives the local mole fractions of refrigerant-11, X_R, and air, $X_A = 1 - X_R$, can be used to determine several required properties of the gaseous mixture. The specific heat ratio of the mixture is given by:

$$\frac{\gamma}{\gamma-1} = X_R \left(\frac{\gamma_R}{\gamma_R - 1}\right) + X_A \left(\frac{\gamma_A}{\gamma_A - 1}\right) . \qquad (A-5)$$

where $\gamma_A = 1.4$ and $\gamma_R = 1.136$. The molecular weight of the mixture is:

$$\mathfrak{m} = X_R \mathfrak{m}_R + X_A \mathfrak{m}_A , \qquad (A-6)$$

where $\mathfrak{m}_A = 28.965$ and $\mathfrak{m}_R = 137.38$. We now determine the mixture gas constant, R, and the refrigerant-11 mass fraction, Y_R, to be:

$$R = 1545/\mathfrak{m} \qquad Y_R = X_R \mathfrak{m}_R/\mathfrak{m} . \qquad (A-7)$$

The static temperature, T, is determined from the energy equation for adiabatic flow in the form:

$$T/T_t = [1 + (\gamma - 1)M^2/2]^{-1} , \qquad (A-8)$$

where T_t, the mixture stagnation temperature, is assumed equal to the initial air plenum temperature. The remaining properties of the mixture are calculated from:

Speed of sound definition $\quad V = M(\gamma RT)^{0.5} \qquad (A-9)$

Equation of state: $\qquad \bar{\rho} = p/RT . \qquad (A-10)$

The mass fraction of the injectant is then given by:

$$(\bar{\rho}V)_R = Y_R(\bar{\rho}V) . \qquad (A-11)$$

ALL LIQUID

The injectant, when it is assumed to occur as all liquid, is further assumed to have a negligible influence on the dynamic and thermal properties of the gas phase (pure air). Then:

$$\gamma = \gamma_A; \, \mathfrak{m} = \mathfrak{m}_A; \, R = 1545/\mathfrak{m}_A , \qquad (A-12)$$

and T, V, and $\bar{\rho}$ are calculated as before to determine the air mass flux, $(\bar{\rho}V)_A$. The mass fraction of refrigerant-11, Y_R, is still given by Eq. (A-7) with $\mathfrak{m}$ given by Eq. (A-6). Then:

$$(\bar{\rho}V)_R = Y_R (\bar{\rho}V)_A /(1 - Y_R) . \qquad (A-13)$$